Chapter 4

Graphene oxide and TiO_2 nanostructures composites for efficient detection of VOCs

4.1 Introduction

Wide variety of nanocomposites having amazing electronic and catalytic properties can be developed by using various nanostructures of carbon such as graphene, carbon nanotubes etc. combined with different metal oxides like TiO_2, SnO_2, ZnO, Cu_2O etc [1-6]. Other forms of graphene like graphene oxide (GO) and reduced graphene oxide (rGO) have been reported numerously to develop nanocomposites combined with distinctive metal oxides [7-12]. Unique properties of graphene like 2-D structure, high electron mobility, chemical stability, huge specific area, ambipolarity in carrier under appropriate field effect etc. have led the researchers globally to explore graphene and its derivatives both experimentally and theoretically [13-15]. Pure graphene has undoubtedly been reported as an excellent material, but graphene oxide due to its electronic structure with highly adjustable bandgap have drawn the attention of many researchers. Various functional groups and ruptured bonds on the surface of graphene oxide sheet makes it soluble in organic and inorganic solvents, thus hybrid or nanocomposites can be easily synthesized with wonderful properties [16-17].

Graphene oxide is made up of sp^2 and sp^3 hybridized carbon atoms [13]. The dominant concentration is of sp^3 hybridized carbon, which is covalently bonded with oxygen in the form of hydroxyl and epoxy groups whereas the left over sp^2 hybridized carbon atoms are bonded with the surrounding carbon or oxygen atoms in form of carboxyl and carbonyl group [18]. Graphene oxide provides a specific bandgap thus providing a favourable and satisfactory electronic property [19]. Many researchers have used nanocomposites of graphene oxide (GO) with metal oxides to investigate the properties of the hybrid, which is valuable in different domains like photocatalysis and hydrogen evolution, [20],[21] H_2 sensing, [22] cellular imaging and drug delivery, [23] ammonia sensing,[8] solar mineralization etc.[24] The nanocomposite formed with graphene as a substrate and metal oxide nanoparticles decorated on it provides excellent properties.[25] In an effort to achieve a high sensitivity in the detection of volatile organic compounds (VOCs), heterojunction of graphene or graphene oxide with different metal oxides like TiO_2, [3] SnO_2, [4] ZnO, [5] Cu_2O etc. [6] have been reported exhibiting excellent properties which are better than sensors fabricated using pure GO and

pure metal oxides. TiO_2 is very much reported and excellent metal oxide for gas sensing because of its wide bandgap, chemical stability, easy synthesis of various nanoforms etc. [26] Highly promising electrochemical and biosensors design by hydrothermally grown TiO_2/graphene nanocomposite was demonstrated by Fan and group [10],[25]. Galstyan and co-workers reported a comprehensive study on reduced graphene oxide/TiO_2 nanotube composite for electrochemical sensing [27]. Lee and group reported sensing of reducing gases at room temperature by GO/TiO_2 composite fabricated using a simple solution method. They also studied the gas sensing behaviour of UV assisted GO/TiO_2 nanocomposite [9]. Li and group reported the synthesis of reduced graphene oxide (rGO) decorated TiO_2 microspherical particles with fine sensitivity and selectivity for ammonia at room temperature [11]. Ye and co-workers demonstrated graphene/TiO_2 hybrid synthesized through hydrothermal method for excellent ammonia sensing at room temperature [28]. Dutta and group fabricated *p*-TiO_2/n-graphene heterojunction prepared by sol gel coating of TiO_2 on CVD grown graphene layer which showed a better selectivity towards H_2 than methane [12].

Also, graphene and its derivatives have been investigated widely to develop field effect devices because of its unique and rich electronics properties. A few reports are available where graphene-derivatives like reduced graphene oxide (rGO) based FETs are reported on flexible substrate for the future electronic applications [29-32]. On the other hand, graphene oxide (GO) and rGO were used as the dielectric material [33],[34] and the channel materials respectively in graphene FET [35] to enhance the device performance effectively.

Owing to the zero-energy band gap of graphene, on/off ratio is observed very low in graphene-based field-effect transistors (GFET) that restricted its acceptability in mainstream electronics [36-38]. Multiple approaches have already been taken to open the band gap in graphene and increase the on/off ratio of GFET. Among all the attempts, the geometric patterning of graphene in the form of nanoribbon (GNR) has mostly been demonstrated where the bandgap has been open by quantum confinement and edge effects to enhance the on/off ratio of GFET [39],[40]. Most of the GNR-FET exhibited an on/off ratio below 100 at room temperature and high at shallow temperature [36],[38],[41-43]. A few articles were found where on/off ratio was reported in-between 600 to 1000 at 300 K for the nano-patterned graphene channel, but no significant transport bandgap was observed in their results in support of the effective turn off of the devices [44],[45]. Also, the applied gate potential was reported to be very high (approximate ±40 V) for GNR-FET that poses a significant drawback of the devices for the use of low power electronics [36],[38],[42],[43],[45].

Also a few reports have been published in the area of graphene field effect transistor (FET) for efficient detection of gases and VOCs. Liu and group have described different methods for the selective detection of NO_2 NH_3, H_2O and CH_3OH using single graphene FET. They have depicted the carrier mobility and gate voltage for each gas in real time [46]. Inaba and group demonstrated ionic liquid gated graphene field effect transistor (ILGFET) for ammonia sensing. They reported the sensing range from 9 to 2400 ppm with good response time at low gate voltage but the response magnitude and the recovery time were according to conventional GFET [47]. Ren and group worked on the detection of SO_2 with graphene FET applied with a large gate voltage (-50V). They have reported a positive Dirac point shift of 1.09 V/ppm to 100 ppm of SO_2 at 100 C with slow recovery of the system (10 min) [48]. Lu and co-workers synthesized rGO FET for ammonia sensing where they achieved quick response/recovery at room temperature but under large positive gate potential (40V) [49]. Some groups reported unique methods like substrate surface modifications [50], doping in GO layer [51] etc. to make the graphene field effect transistor (GFET) more appropriate for gas/vapor sensing applications.

FET structured gas/vapor sensors also showed multiple advantages due to the application of gate voltage as mentioned by the Liu and co-workers. They proposed a new method for the selective detection of different gases/VOCs like NO_2, NH_3, H_2O and CH_3OH by using the conductance vs gate voltage characteristics of GFET sensor [46]. Lu and group reported efficient ammonia sensing at room temperature by GFET sensor applying a suitable gate voltage. They also depicted an immediate response and recovery of the sensors in p mode (hole majority) and repeatable sensor operation in n mode (electron majority) [49]. Falak and group reported a highly selective NH_3 sensing based on the TiO_2-graphene hybrid FET. In the same hybrid FET sensor, high response magnitude with full recovery at room temperature was observed under a suitable gate bias [52]. Except gas sensing, TiO_2 loaded graphene field effect transistor (GFET) was also reported versatile applications. Graphene field effect transistor decorated with TiO_2 nanoparticle successfully used for the ultraviolet detection [53],[54]. A few other reports shows promising photoresponse in single layer graphene FET decorated with TiO_2 nanoparticle [55-57].

In this chapter, two different types of GO-TiO_2 nanostructures composites with their detailed characterizations and VOC sensing performance have been represented. GO loaded TiO_2 nanotube composite was fabricated by simple electrochemical anodization route. Uniform doping across the nanotubes was achieved with the help of anodization. GO loaded TiO_2

nanotube composite sensor was fabricated having sandwich structured and tested against methanol vapours at room temperature.

GO-*p*-TiO_2 nanoparticles composite channel based back gated FET sensors were developed for the detection of volatile organic compounds (VOCs) of very low concentrations. Graphene being ambipolar in nature exhibits FET behaviour. This FET behaviour is thoroughly studied in pure graphene oxide and *p*-type anatase TiO_2 nanoparticles implanted single layer graphene oxide through electrical characterization. Current-voltage (I_D-V_{GS}) characteristics were measured for the samples including the pure TiO_2 nanoparticles, pure graphene oxide and nanocomposites. I_{ON}/I_{OFF} ratio, transconductance and mobility was measured for GO-*p*-TiO_2 nanoparticle composite and compared with pure graphene oxide. Detection of VOC was performed at V_{GS}= 0 V and under positive gate bias also (VGS > 0 V). I_D-V_{GS} characteristics were measured for nanocomposite samples which depicted adequate ambipolar behaviour in two different ambient i.e. air and 100 ppm ethanol at $V_{DS} = 0.5\,V$ at 100°C and their corresponding response magnitude was calculated for variable V_{GS}. The field assisted sensitivity amplification technique was applied in GO-*p*-TiO_2 NPs FET sensor for enhancing the lower detection limit of the VOCs significantly.

4.2 GO loaded TiO_2 nanotube array

4.2.1 Synthesis

Pure TiO_2 nanotubes (S_0) were synthesized by electrochemical anodization method which has been discussed in section 2.2.1 of chapter 2. Graphene (supermarket brand) aqueous solution synthesis procedure discussed in section 2.4.1 of chapter 2. of 500 lit was added in the previous electrolyte for synthesizing GO-TiO_2 nanotube composite (S_1).

Nanocomposite preparation

An electrolyte was prepared with 0.5 wt% NH_4F, 10 vol% of GO aqueous solution and ethylene glycol for the preparation of graphene loaded TiO_2 nanotubes array. Again, the anodization was performed for 120 min by applying a constant voltage of 40 V. Due to the constant availability of GO in the electrolyte, graphene was doped uniformly in the TiO_2 nanotubes.

4.2.2 Characterizations

Morphological Characterization

FESEM images of pure (S_0) and GO loaded (S_1) TiO_2 nanotubes array had no significant morphological variation. Both the samples offered ordered and oriented TiO_2 nanotubes array

without any significant change due to GO loading. Similar nanotubes images were observed for GO loaded TiO2 nanotubes as depicted in Fig. 2.1.

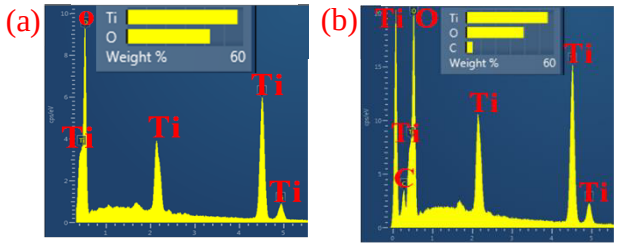

Fig. 4.1. EDS Spectra: (a) pure TiO_2 nanotubes array (S_0) and (b) GO loaded TiO_2 nanotubes array (S_1).

To the study the chemical composition of pure TiO_2 nanotube and GO loaded TiO_2 nanotube array EDS was done. EDS spectra confirm the formation of TiO_2 showing the existence of Ti and O in the Fig. 4.1(a) and (b). The existence of carbon in the sample S_1 is clearly envisaged from EDS spectra shown in the inset of Fig. 4.1(b).

Structural characterization

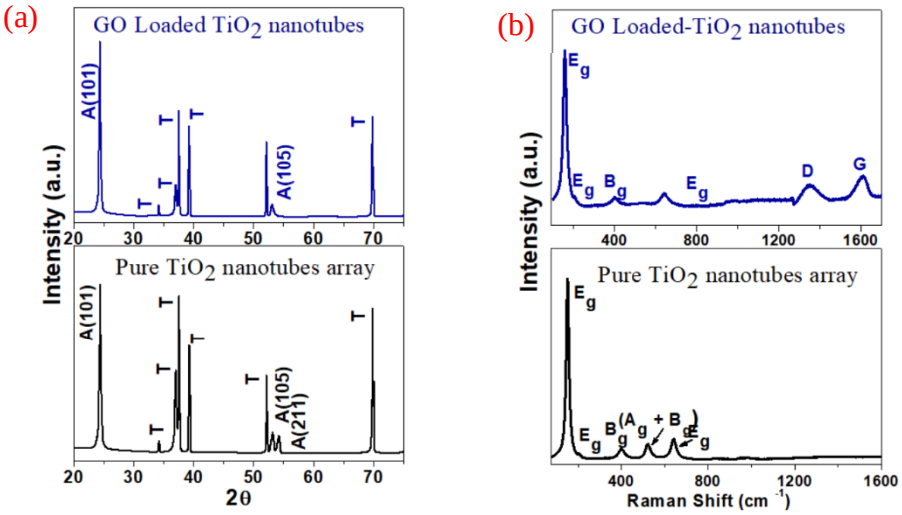

Fig.4.2. (a) XRD spectra and (b) Raman spectra of pure TiO_2 nanotubes array (S_0) and GO loaded TiO_2 nanotubes array (S_1).

A high-intensity peak of anatase (101) crystallinity at 25.3º and low-intensity anatase (105) peak is observed in both the samples (Fig.4.2 (a)). Low-intensity anatase (211) peak is shown in S_0 but invisible in S_1 samples. Additional Ti peaks, originated due to the presence of Ti substrate, are almost similar for both the S_0 and S_1 sample. The intensity of Ti peaks is relatively less compared to the anatase (101) in case of GO loaded samples (i.e. S_1). The anatase peak A (211) is only present in the S_0 sample showing that more anatase phase is present in the pure TiO_2 nanotube array than in GO loaded TiO_2 nanotube.

Raman spectra were recorded at room temperature (300 K) using a 532 nm laser to study the composition of S_0 and S_1 samples. The Raman spectra of both the samples were compared. Also, the common modes situated at 144 cm^{-1} (E_g), 197 cm^{-1} (E_g), 399 cm^{-1} (B_g), 516 cm^{-1} (A_g + B_g) and 639 cm^{-1} (E_g) corresponds to the pure anatase TiO_2 (Fig. 4(a) and (b)). The main high intensity peak located at 144 cm^{-1} (Eg) describes the Ti-O bond formed in the anatase phase of TiO_2 nanotubes. Two bands located at 1348 cm^{-1} (D) and 1600 cm^{-1} (G) corresponds to graphene for S_1 sample (Fig. 4.2(b)). The Raman bands of anatase TiO_2 and graphene confirms to their respective positions even after the loading of GO in the sample S_1.

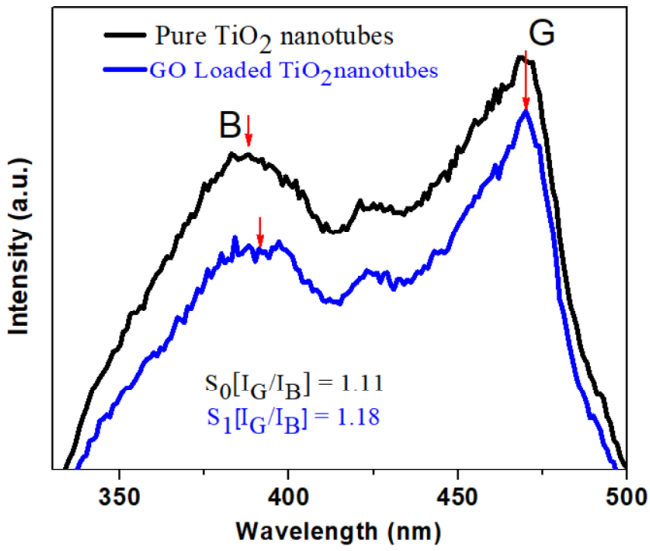

Fig. 4.3 Photoluminescence spectra of pure TiO_2 nanotubes array (S_0) and GO loaded TiO_2 nanotubes (S_1) at 300 nm of excitation.

The photoluminescence spectra of both the samples were recorded at an excitation of 300 nm at room temperature (300 K). The lower peak intensities of GO-loaded TiO_2 indicate the less recombination rate of photo-induced electron-hole pair as compared to the plane TiO_2 nanotube (Fig. 4.3). Peak B (near 388 nm) in the UV region corresponds to the direct and indirect band to band recombination. Peak G (near 470 nm) in the visible region indicates the shallow trap levels that are associated with the oxygen vacancies stated below the conduction band [3, 40]. Two significant changes are observed in PL spectra in Fig. 4.3 i.e. (i) a right shift of band-to-band emission peak (peak B) in case of S_1 compared to S_0 and (ii) increment in the intensity ratio of peak G and peak B for S_1 compared to S_0. Right shift of peak B confirms lesser band gap and high-intensity ratio (I_G/I_B) confirms the existence of more defects for GO-doped TiO_2 nanotubes array compared to the pure one.

4.2.3 Device fabrication

Vertical (MIM) device structure was fabricated for GO-TiO_2 nanotube composite as considered for pure TiO_2 nanotube array. Metal insulator metal (MIM) device structure was explained in detail in chapter 3 (section 3.2.3).

4.2.4 VOC sensing

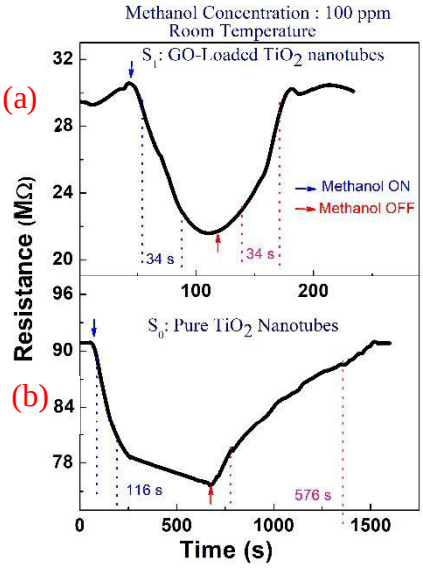

Fig. 4.4. Transient behaviour in exposure to 100 ppm methanol at room temperature of (a) GO-loaded TiO_2 nanotubes, (b) pure TiO_2 nanotubes.

The fabricated sensors using two different types of TiO_2 nanotubes array i.e. S_0 and S_1 were used for methanol sensing. Both the sensors (S_0 and S_1) were exposed to 100 ppm of methanol at room temperature (300 K). The baseline resistance of sample S_0 and S_1 was measured as 90.7 MΩ and 30 MΩ respectively (Fig. 4.4). Presence of GO in TiO_2 increased the overall conductivity compared to the pure one. GO was responsible for more defects in TiO_2 authenticated from PL study. Enhanced mobility was also expected in the GO loaded TiO_2 nanotubes array compared to the pure nanotubes.

However, *n*-type conductivity (electron dominating) was observed for both the samples and sensor resistance was decreased in presentence of reducing vapor methanol. In the exposure of 100 ppm of methanol, sensor resistance of S_0 was decreased from 90.7 MΩ to 75.4 MΩ and S_1 was dropped from 30 MΩ to 21 MΩ. So, corresponding response magnitude ($\Delta R/R \times 100$) of S_0 and S_1 were calculated and found to be ~20 % and ~28 % respectively. The fall time and rise time of sample S_0 is 116 s and 576 s respectively. The sample S_1 (GO loaded TiO_2 nanotube array) has better fall time and rise time that is 34 s and 34 s.

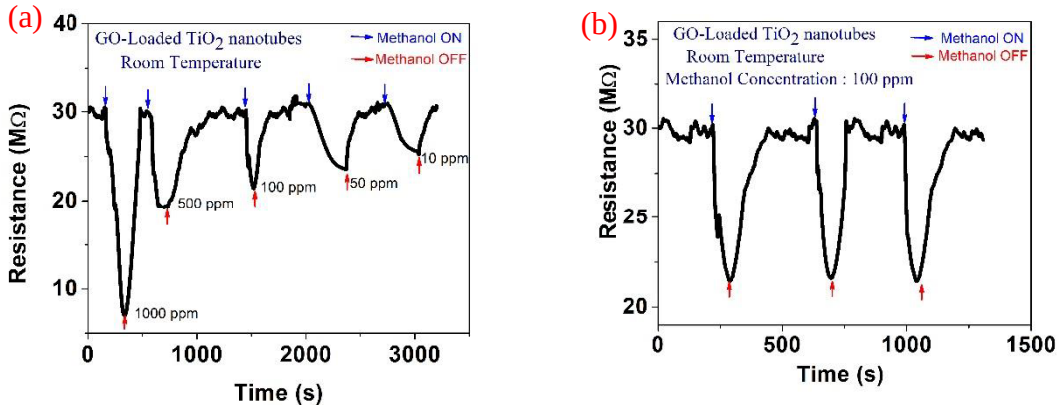

Fig. 4.5. GO- loaded TiO_2 nanotubes (a) transient response behaviour within the concentration range of 10 to 1000 ppm, (b) repeated cycles in the exposure to 100 ppm of methanol at room temperature.

These parameters show that sensor response has been improved in case of a GO loaded TiO_2 nanotube array than in pure TiO_2 nanotube array. Transient response behaviour of S_1 sensor was obtained from a concentration range of 1000 ppm to 10 ppm of methanol at room temperature (Fig. 4.5(a)). Detection till 10 ppm was achieved with a fair response magnitude of 19 %. S_1 sensor depicted a stable baseline resistance with highly repeatable transient behaviour at room temperature (Fig. 4.5(b)). Sensor response was increased with short response and recovery time also in case of GO loaded TiO_2 nanotube (S_1) compared to the plane nanotube sensors at room temperature (300 K).

4.2.5 Sensing mechanism

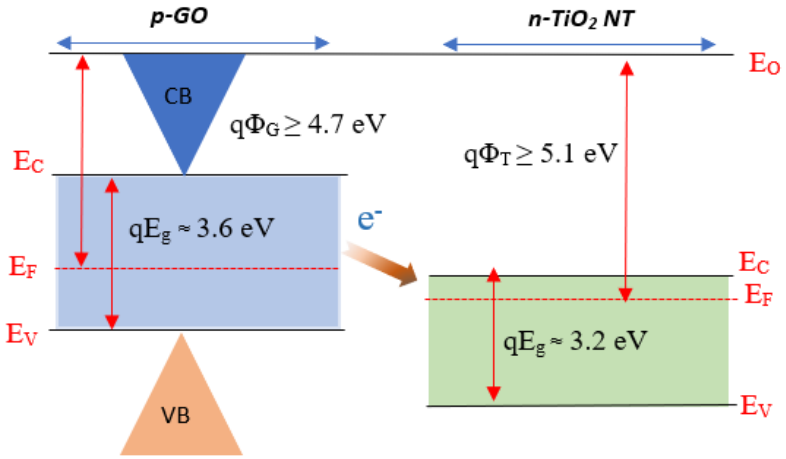

Fig. 4.6. Heterojunctions are formed between *p*-type GO and *n*-TiO_2 nanotubes.

The 2-D layered structure and large surface area of graphene oxide improve the gas sensing performance when incorporated in TiO_2 nanotubes array. Good electrical conductivity and high mobility of charge carriers were observed in case of S_1 that eventually decreased its resistance

as compared to S_0 sensor. The sensitivity of the GO loaded TiO_2 nanotube sample was greater than the pure TiO_2 nanotube sample. Presence of graphene had enabled the sensing device to work at room temperature.

Energy band diagram of *p*-GO and *n*-TiO_2 have been sketched by considering the work function of GO $q\varphi_{GO} \geq 4.7\ eV$ [58] and anatase *n*-TiO_2 $q\varphi_{TiO2} \geq 5.1\ eV$ [59]. Energy band gaps of 3.59 eV for pure GO and 3.2 eV for pure TiO_2 (S_0) were estimated from the UV vis spectra represented in chapter 2. On the formation of heterojunction between TiO_2 and GO, electrons are transferred from GO to TiO_2 and get accumulated on the TiO_2 surface. Therefore, conductivity of TiO_2 nanotube, after GO loading was increased lowering the base line resistance as evidenced from Fig. 4.5.

$$O_2(gas) \rightarrow O_2(absorbed) \tag{4.1}$$

$$O_2(absrorbed) + e^- \rightarrow O_2^- (absorbed) \tag{4.2}$$

$$O_2^- + e^- \rightarrow 2O^-(adsorbed) \tag{4.3}$$

Surface adsorption of oxygen groups (O_2^-, O^-, O^{2-}) reduces the electron concentration (Eq.4.1-4.3). In air ambient, electron concentration in TiO_2 is decreased due to the availability of the oxygen species in large number. However, electron deficiency in TiO_2 nanotubes extracts more electron from GO, increasing the width of surface depletion region. On exposure to methanol vapours, the trapped electrons oxygen groups are released back to the surface of TiO_2 nanotube array sensor, enhancing the conductivity.

$$CH_3OH + O^- \rightarrow HCOH + H_2O + e^- \tag{4.4}$$

$$CH_3OH + O_2^- \rightarrow HCOOH + H_2O + e^- \tag{4.5}$$

When methanol vapours reacts with the oxygen species it gets oxidised into formaldehyde and afterwards to formic acid and then releases electrons to conduction band, which in turn reduces the resistance of the sensor in exposure to methanol vapours (Eq.4.4 and 4.5) [60].

Formation of depletion regions across the TiO_2 and GO junction plays an important role for improving the sensor response. Uniform loading of graphene oxide on the TiO_2 surface can be considered as the main reason for enhancing the change of current in-between air and VOC ambient that eventually shows high sensitivity towards methanol by the graphene doped TiO_2 nanotube sensor at room temperature with quick response time and recovery time.

4.3 GO-*p*-type TiO_2 nanoparticle composites

4.3.1 Synthesis

Undoped *p*-type TiO_2 nanoparticles were prepared by sol-gel method as described in section 2.3.1 in chapter 2. The preparation of aqueous solution of graphene oxide solution is explained in section 2.4.1 of chapter 2.

Nanocomposite preparation

Seven different nanocomposites (S_2-S_8) were prepared by varying the ratio (in volume percent) of both TiO_2 nanoparticles and GO as represented in Table 4.1. A total of nine samples were prepared including the pure TiO_2 NPs (S_1), nanocomposites (S_2-S_8) and pure GO (S_9).

Table 4.1 Details of the sample (S_1-S_9)

Sample number	Solution of TiO_2 NPs (2ml TTIP + 10 ml CH_3COOH+ 40 ml H_2O)	0.2 wt% Solution of single layer GO flakes	Type of materials
S_1	100 vol%	0 vol%	Pure TiO_2
S_2	99 vol%	1 vol%	Composite
S_3	95 vol%	5 vol%	Composite
S_4	90 vol%	10 vol%	Composite
S_5	50 vol%	50 vol%	Composite
S_6	10 vol%	90 vol%	Composite
S_7	5 vol%	95 vol%	Composite
S_8	1 vol%	99 vol%	Composite
S_9	0 vol%	100 vol%	Pure GO

4.3.2 Characterization

Morphological characterization

The *p*-TiO_2 NPs and GO solutions were prepared in such a way, the formation of nanocomposite has neither distrusted the morphology of TiO_2 nanoparticles nor the graphene oxide as confirmed from FESEM and TEM image in Fig. 4.7.

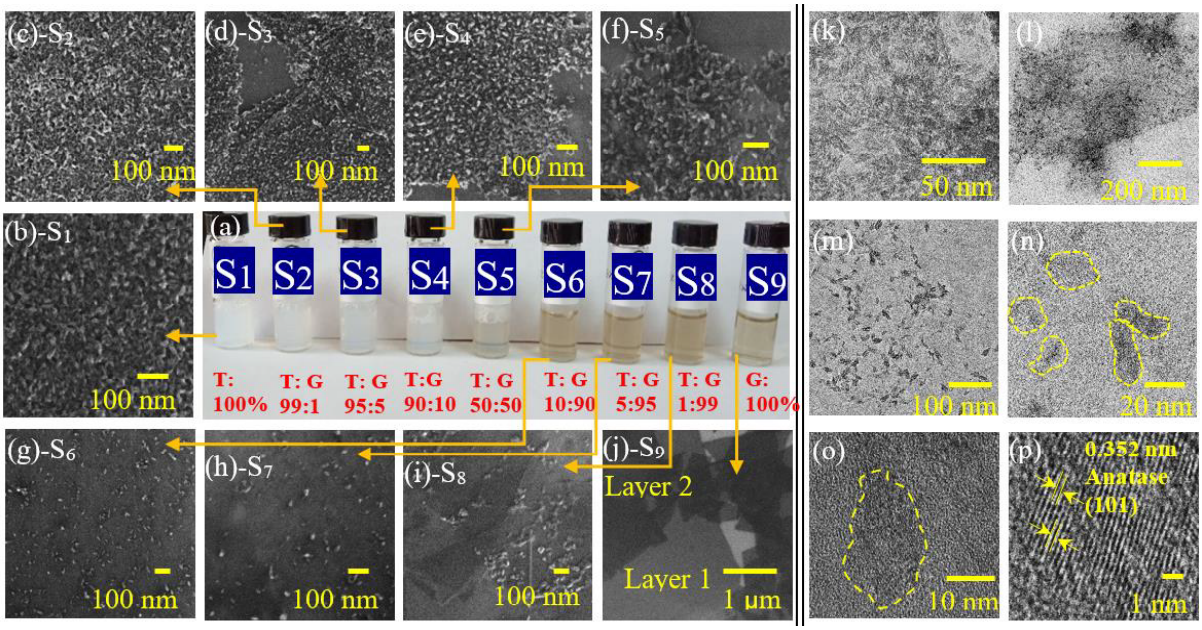

Fig. 4.7. FESEM and TEM images of *p*-TiO_2 nanoparticles (NPs) embedded graphene oxide (GO) on SiO_2/Si substrate. (a) homogeneous mixture of TiO_2 and GO (T:G) in different ratio including pure solution of TiO_2 NPs (T:100%) and GO (G:100%)). FESEM image of (b) S_1: pure *p*-TiO_2 NPs, (c) S_2: 1 vol% GO loaded 99 vol% of *p*-TiO_2 NPs, (d) S_3: 5 vol% GO loaded 95 vol% of *p*-TiO_2 NPs, (e) S_4: 10 vol% GO loaded 90 vol% of *p*-TiO_2 NPs, (f) S_5: 50 vol% GO mixed with 50 vol% of *p*-TiO_2 NPs, (g) S_6: 10 vol% *p*-TiO_2 NPs embedded 90 vol% of GO, (h) S_7: 5 vol% *p*-TiO_2 NPs loaded 95 vol% of GO, (i) S_8: 1 vol% *p*-TiO_2 NPs loaded 99 vol% of GO, (j) S_9: pure GO flakes. TEM images of (k) pure *p*-TiO_2 NPs, (l) *p*-TiO_2 NPs decorated on GO flakes, (m) magnified TEM image of *p*-TiO_2 NPs decoration on GO, (n) *p*-TiO_2 NPs marked with oval shape dotted line showing an average size of ~12 nm, (o) lattice image of single *p*-TiO_2 nanoparticle on GO, (p) HRTEM lattice image of anatase *p*-TiO_2 with a d-spacing of 0.352 nm.

Uniform, continuous and compact distribution of *p*-TiO_2 NPs was observed in S_1 and S_2 (Fig. 4.7(b) and (c)). S_3, S_4 and S_5 exhibited densely occupied *p*-TiO_2 NPs on GO flakes but the separation of NPs was increased gradually from S_3 to S_5 (Fig. 4.7(d) and (f)). The uniform separation of *p*-TiO_2 NPs is very much clear in S_6 and the separation is increased further in S_7 and S_8 (Fig. 4.7(g-i)). FESEM image of S_9 confirms the formation of mostly single layer of pure GO flakes (Fig. 4.7(j)). However, the FESEM images in Fig. 4.7 successfully discriminate the TiO_2 dominated samples (i.e. S_1 to S_5) and GO dominated samples (i.e. S_6 to S_9). The uniform distribution of *p*-TiO_2 NPs without and with GO flakes was further authenticated by the TEM image in Fig. 4.7(k), (l) and (m). ~12 nm average size of TiO_2 NPs was estimated from a high resolution TEM image in Fig. 4.7(n) and (o). The d-spacing of 0.352 nm measured from lattice image in Fig. 4.7(p) confirmed the formation of anatase (101) crystallinity.

Structural characterization

Raman spectroscopy scan, from 100 cm^{-1} to 700 cm^{-1} (for anatase TiO_2) and 1200 cm^{-1} to 1800 cm^{-1} (for GO) are shown separately in Fig. 4.8(a) and Fig. 4.8(b) respectively. The presence of anatase crystallinity in *p*-TiO_2 NPs was confirmed by Raman modes like E_g (144 cm^{-1}), E_g (199 cm^{-1}), B_g (399 cm^{-1}) and E_g (639 cm^{-1}). The diminishing of these peaks from S_1 to S_8 and elimination in S_9 is also visible clearly in Fig. 4.8(a). [61] The appearance of the D and G peak from samples 2 to sample 9 is depicted in Fig. 4.8(b). The ratio of D and G peak intensity (I_D/I_G), calculated from Fig. 4.8(b) was increased gradually from S_9 to S_2 as shown in Fig. 4.8(e-i). So, the synthesized nanocomposite leads to the formation of more sp^3 carbon defects [61], [62].

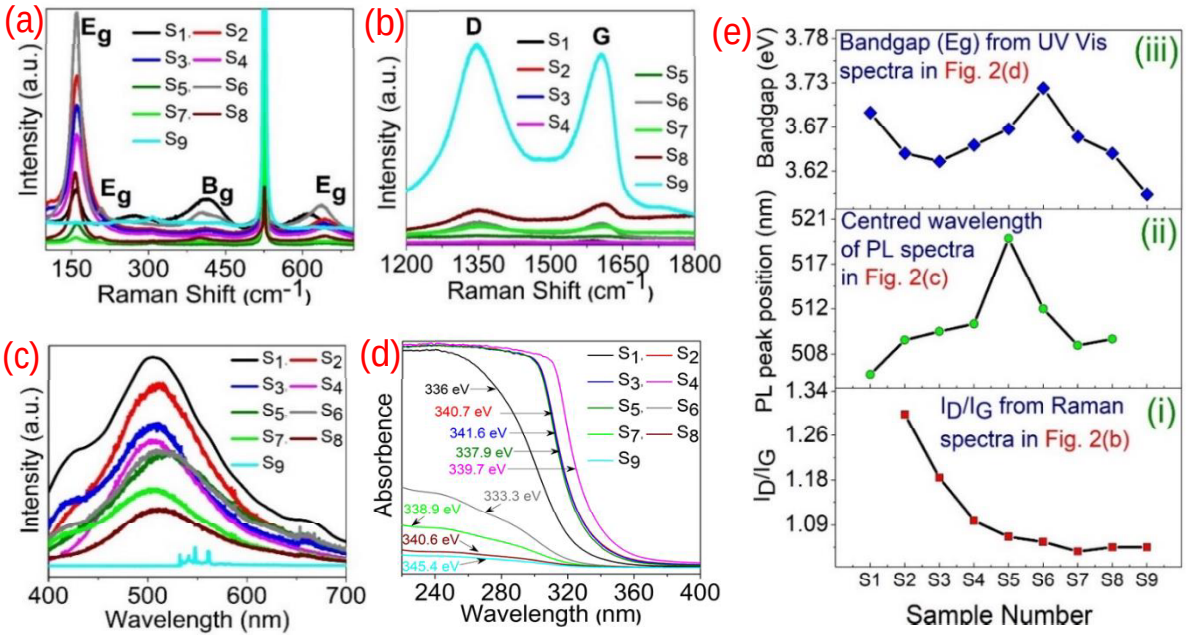

Fig. 4.8. Structural analysis of S_1-S_9. Raman spectra measured under 500 nm laser at room temperature (300 K) shows (a) 100-700 cm^{-1} scan for anatase and (b) 1200-1800 cm^{-1} scan for GO. (c) Photoluminescence (PL) spectra showing a shifting of peak position in visible region, (d) UV Vis spectra of all the samples to estimate absorption edge, (e) sample wise variation of I_D/I_G from Raman spectra (i), centered wavelength shifting from PL spectra (ii) and band gap variation from UV Vis spectra (iii).

This increased ratio of I_D/I_G can also be attributed to the formation of Ti-O-C bond. The high intensity peak at around 525 cm^{-1} (Fig. 4.8(a)) is visible in all the samples is attributed to silicon as the SiO_2/Si was the common substrate for all the samples.

PL peak intensity in the visible range was maximum for S_1 (pure *p*-TiO_2) and decreased gradually from S_1 to S_8 with increase of GO level in the nanocomposite and minimum for S_9 (pure GO) as shown in Fig. 4.8(c). The heterojunction formed between the GO and TiO_2 NPs

results in increased separation rate of electron hole pairs in which graphene attracts the electrons and holes gets accumulated on the surface on TiO_2 nanoparticles [63], [64]. This deter the recombination of holes and electrons decreasing the PL intensity of the TiO_2/GO nanocomposites [63]. Also, the formation of Ti-O-C bond extends the light absorption wavelength in the visible region. Centered absorption wavelength was found at 503 nm for S_1, shifted maximum up to 519 nm for S_5 and back to 508 nm for S_8 as shown in Fig. 4.8(e-ii). Ti-O-C linkage formation was maximum for S_5 due to the appropriate ratio of TiO_2 and GO showing a maximum shift towards the visible region. Whereas, S_1 was pure TiO_2 and S_8 was dominated by the concentration of GO showed lower value centered absorption wavelength in the visible region.

The absorbance is high and almost constant in the TiO_2 dominating samples (S_1-S_5) and decreased gradually in GO dominating samples (S_6-S_9) as depicted in UV Vis spectra in Fig. 4.8(d). The pure TiO_2 nanoparticles (S_1) has an absorption edge at 336 nm while pure graphene oxide represents its absorption edge at 345 nm. When, the TiO_2 NPs dominated samples (S_2-S_5) have a shift towards the higher wave number due to the formation of Ti-O-C bond, GO dominated samples (S_7-S_9) have a shift towards the lower wave number due to restricted TiO_2 NPs on GO with limited Ti-O-C linkage. Thus, when the graphene oxide solution is mixed with TiO_2 nanoparticles, some of its unpaired Π electrons forms a bond with free electrons that are available on the surface of TiO_2 nanoparticles. On the formation of nanocomposite, the graphene oxide and TiO_2 nanoparticles adjust their fermi level and thus modifying the bandgap of the nanocomposite [65]. However, two composites i.e. S_5 and S_6 exhibited very high bandgap of 3.7 eV and 3.72 eV respectively which was greater than pure TiO_2 NPs (S_1: 3.69 eV) and pure GO (S_9: 3.59 eV) shown in Fig. 4.8(e-iii).

Chemical characterization

Splitting of photoelectrons of Ti^{4+} is assigned to $Ti2p_{3/2}$ and $Ti2p_{1/2}$ with a separation of 6 eV that authenticate the existence of anatase TiO_2 in S_1, S_3 and S_8 whereas noisy spectrum conforms the absence of TiO_2 in pure GO in S_9 (Fig. 4.9(a)) [66].

Pure TiO_2 NPs (S_1) exhibited C1s level due to the availability of carbon impurities originated from the Titanium (IV) isopropoxide and CH_3COOH during synthesis of TiO_2 NPs by chemical route. Carbon impurities in pure TiO_2 (S_1) exhibited two clear peaks at 284.5 eV and 286.3 eV with a hump at 288.3 eV as shown in Fig. 4.9(b) [67]. The peak intensity at 284.5 eV (C-C and C=C) was increased in the *p*-TiO_2/GO nanocomposites (i.e. S_3 and S_8) and was maximum in pure GO (S_9) due to increase of sp^2 hybridize carbon atom [68]. Oxygen functionalized carbon,

such as hydroxyl/epoxy (C-O) peak was located at 286.1 eV and found for all the samples as shown in Fig. 4.9(b) [69]. High intensity peak at 288.3 eV for *p*-TiO_2 /GO nanocomposites (i.e. S_3 and S_8) is believed to originate from Ti-O-C linkage due to substitution of carbon atom for some of the lattice Ti atoms [70],[71]. The strong Ti-O-C peak in C1s spectrum of S_3 and S_8 also reveals the bonding creation by electronic exchange between TiO_2 and GO authenticating the good quality hybrid formation. Other oxygen functional groups, such as C=O and COOH were found for pure GO (S_9). The small hump in S_1 (Fig. 4.9(b)) near 288 eV possibly contributed by Ti-O-C and oxygen functionalized carbon groups like COOH etc. [67], [69].

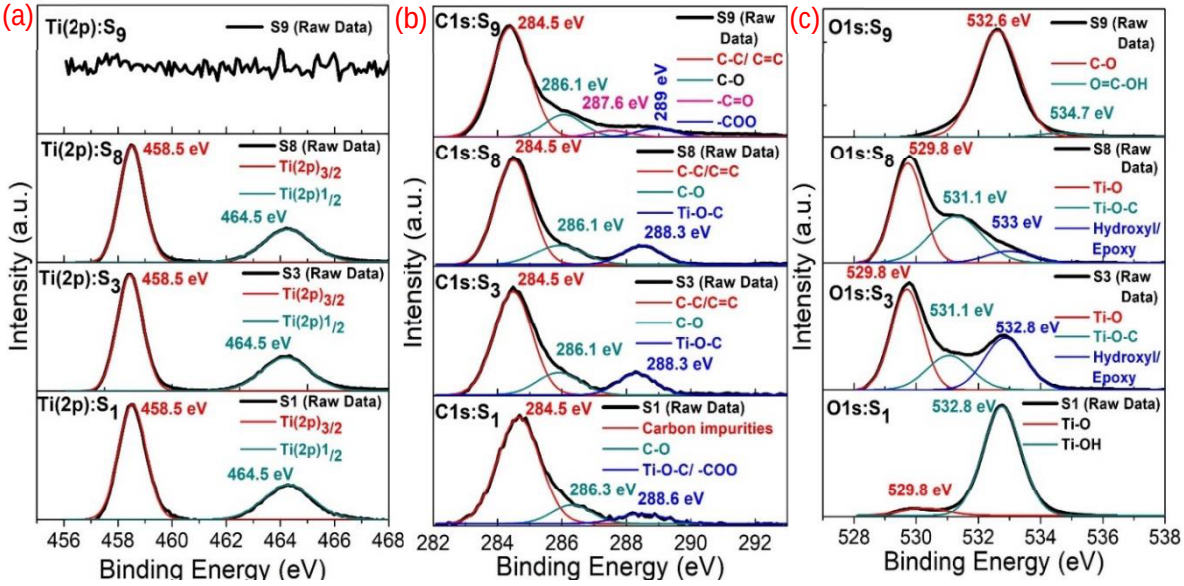

Fig. 4.9. XPS spectrum of four selective samples among the nine i.e. S_1 (pure *p*-TiO_2 NPs), S_3 (95 vol% *p*-TiO_2+5 vol% GO), S_8 (1 vol% *p*-TiO_2+ 99 vol% GO) and S_9 (pure GO). (a) Ti2p doublet peaks for S_1, S_3 and S_8. Being a pure GO sample, no Ti2p peaks were observed for S_9. (b) C1s spectrum; S_1, S_3, and S_8 are deconvoluted in three peaks, originated from sp^2 carbon (C-C, C=C), ether (C-O) and Ti-O-C linkage. Additional C=O and COOH peaks were observed for pure GO (S_9) without Ti-O-C peak at 288.3 eV. (c) O1s spectra of pure *p*-TiO_2 NPs (S_1) showed high and low intensity oxygen peak from surface oxygen (Ti-OH) and TiO_2 crystal (Ti-O). O1s spectrum were deconvoluted in three peaks (Ti-O, Ti-O-C and hydroxyl/epoxy) for S_3 and S_8. Strong O1s spectra at 432.6 V for pure GO (S_9) originated from hydroxyl/epoxy groups are available on GO surface.

O1s spectra of pure TiO_2 (S_1) exhibited high intensity peak at 532.8 eV attributed to the surface oxygen originated from Ti-OH, organic impurities, adsorbed oxygen species etc. whereas Ti-O peak intensity at 529.8 eV was quite low (Fig. 4.9(c)) [68],[72]. The unusually high peak intensity at 532.8 eV in S_1 was observed due to the extremely small dimensions (~12 nm) of the particles that eventually increased the number of surface atom reducing the bulk formation

that results a high intensity surface oxygen peak compared to the bulk oxygen (Ti-O). The engagement of free electrons in surface adsorption by oxygen species, -OH etc. exhibited that hole majority in the TiO_2 NPs showing *p*-type conductivity [73]. O1s spectrum was deconvoluted in three peaks attributed to Ti-O at 529.8 eV, [11] Ti-O-C at 531.1 eV [67], [74] and surface oxygen (hydroxyl/epoxy) at 532.8 eV [75] for *p*-TiO_2/GO nanocomposites (i.e. S_3 and S_8) (Fig. 4.9(c)). As compared to S_1, relative peak intensity of surface oxygen and bulk oxygen was changed significantly in case of S_3 and S_8 due to (i) increment of *p*-TiO_2 in GO and (ii) formation of Ti-O-C linkage. The existence of strong Ti-O-C peaks in both the C1s and O1s spectrum for S_3 and S_8 confirmed the electron transfer between *p*-TiO_2 and GO supporting the formation of *p*-TiO_2 /GO nanocomposites [74]. Strong O1s peak at 532.6 eV originated from pure GO (S_9) due to presence of oxygen functionalized groups (mainly, hydroxyl/epoxy) on GO surface [68].

4.3.3 Device fabrication

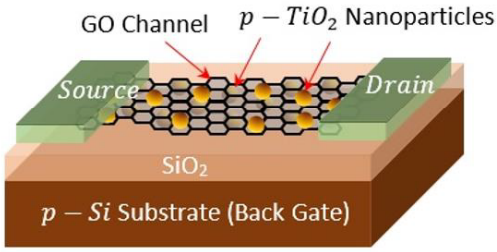

Fig. 4.10. Schematic of back gated field effect transistor (FET) having *p*-TiO_2 NPs embedded GO channel.

Boron-doped, ~500 µm thick <100> SiO_2/Si wafer having SiO_2 thickness of 90 nm was used as the substrate where resistivity of Si was 0.001-0.005 Ω-cm. All the samples including the pure TiO_2 NPs (S_1), nanocomposites (S_2-S_8) and pure GO (S_9) were sonicated for 15 min and then deposited on cleaned SiO_2/Si wafer (5 mm × 5 mm) by dip coating technique (Appex Instruments: Xdip-SV-1). All the samples were subsequently kept for annealing at 250 °C for 5 hours.

p-TiO_2 embedded graphene oxide field effect transistors (FETs) were fabricated on SiO_2/Si substrate which is specified in the previous paragraph. SiO_2 layer of the back side of the substrate was etched selectively (1 mm×1 mm) by HF to create gate contact from *p*-Si by using negative photoresists. Au drain and source electrodes of thickness 150 nm was deposited on *p*-

TiO_2/GO nanocomposites coated SiO_2/Si substrate with a separation of ~1 mm by electron beam evaporation method using Cu physical mask (Fig. 4.10(c)).

4.3.4 Electrical characterizations

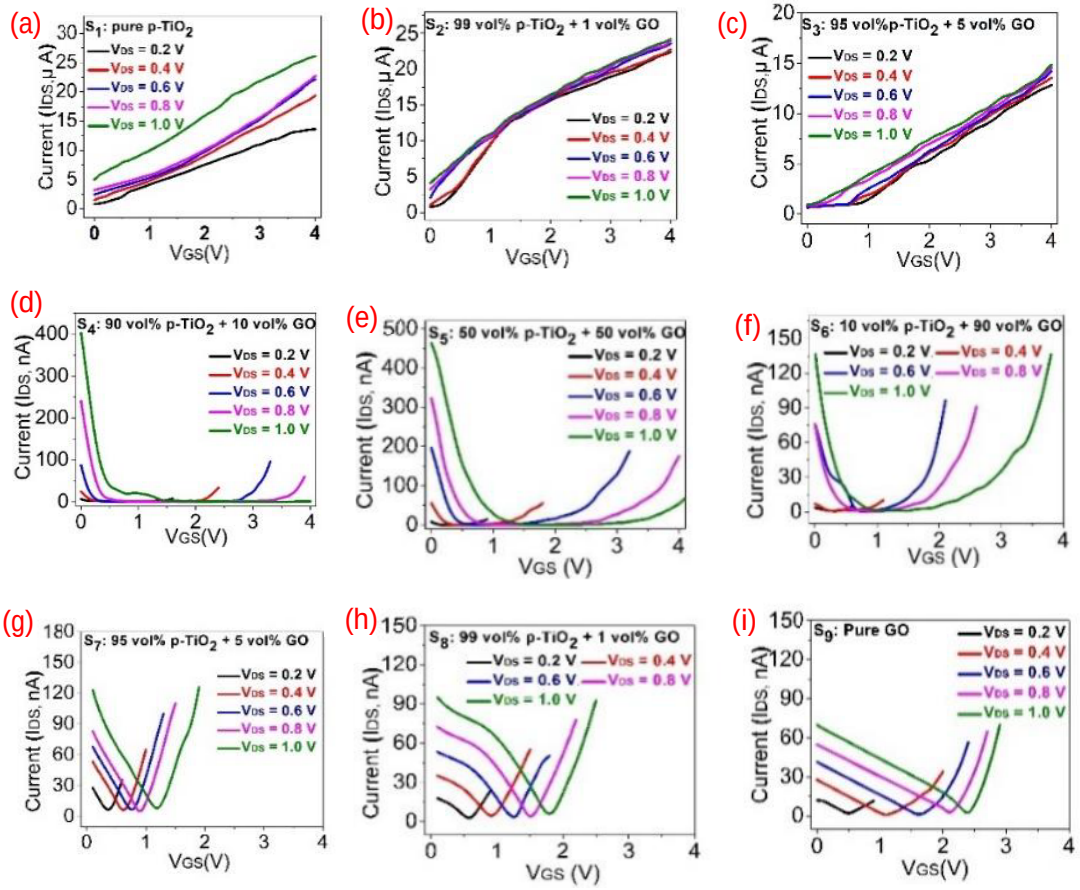

Fig. 4.11. Transfer characteristics (I_{DS}- V_{GS}) of *p*-TiO_2/GO FETs with variable V_{DS} (0.2-1 V) for (a) S_1, (b) S_2, (c) S_3, (d) S_4, (e) S_5, (f) S_6 (g)S_7, (h)S_8 and (i)S_9. No significant field effect was observed in S_1 to S_3.

All the FETs were tested at positive gate voltage ($V_{GS} > 0$) where drain current was controlled by the field effect. Graphene oxide exhibits ambipolar transport in field effect devices structure where the majority charge carrier in 2-D channel can change from holes to electron due to application of appropriate gate voltage [15],[50].

The field effect was studied for all the samples (S_1 to S_9) where only GO dominated samples (S_4 to S_9) exhibited ambipolar behaviour in the transfer characteristics (I_{DS}- V_{GS}) for various V_{DS} (0.2 to 1 V) as shown in Fig. 4.11. Whereas the TiO_2 nanoparticles dominated samples (S_1-S_3) did not show any ambipolar behaviour. They depicted linear current- voltage characteristics for different V_{DS} (0.2 to 1 V) (Fig. 4.11(a-c)). Pure GO-FET (S_9) along with S_8 and S_7 exhibited

'V' shaped transfer characteristics confirming strong control of the gate voltage over the drain current (Fig. 4.11(g), (h) and (i)). On the other hand, transfer characteristics became 'U' shaped with increase of TiO_2 ratio in the GO channel possibly due to the formation of more *p*-TiO_2 NPs/GO heterojunctions in the channel (Fig. 4.11(d),(e) and (f)).

All the FETs showed depletion mode operation i.e. on-current at $V_{GS} = 0$ and the current was decreased with the increase of V_{GS} in a positive direction. Minimum (off) current at $V_{GS} = V_{Dirac}$ was recorded below 1.5 V for all the FETs while the complete transfer characteristics of all the devices were recorded in the range of $0 \leq V_{GS} < 4$ V.

Due to application of field assisted doping of $n(V_{GS})$, electron concentration increases towards positive V_{GS} dropping the effective hole concentration in GO [25],[26] and the devices shows "V"-shape transfer characteristics (I_{DS}-V_{GS}) with a minimum charge density point (V_{Dirac} or Dirac point) with lowest drain current (I_{DS}) [17]. The $n(V_{GS})$ can be expressed as $n(V_{GS}) = \left(\frac{C_G}{q}\right) \times V_{GS}$ where the gate capacitance $C_G = \frac{\varepsilon_0 \varepsilon_r}{t_{ox}}$. ε_0 is the permittivity of free space, ε_r is the dielectric constant of SiO_2 (~3.9), t_{ox} is SiO_2 thickness (90 nm) and q is unit charge of electron. At $V_{GS} > V_{Dirac}$, electrons become the majority carrier with a rapid increment of I_{DS}.

High I_{ON}/I_{OFF} ratio measurement

However, on/off ratio of pure graphene oxide (S_9) was recorded as 66 at 300 K. Initial current level and non-linearity in $I_D - V_{GS}$ both were increased in GO/TiO_2 hybrid FETs (Fig. 4.12(a)). On/off current ratio was calculated as 700, 2800, and 1350 for S_8, S_7, and S_6 at room temperature, respectively (Fig. 4.12(b) and (c)). ~42 times increment in the on/off ratio was recorded for S_7 as g_m of S_7 was appreciably high, i.e. 0.286 µS (Fig. 4.12(d)). $I_D - V_{DS}$ characteristics of all the FETs were tested within ±2 V while the devices were 'on' i.e. V_{GS}=0 (Fig. 4.12(e)). $I_D - V_{DS}$ in Fig. 4.12(e) exhibited a noticeable similarity with $I_D - V_{GS}$ in terms of linearity. S_9 exhibited a complete linear $I_D - V_{DS}$ and the non-linearity was increased gradually from S_8 to S_7 to S_6 (Fig. 3.10(e)).

The effect of variable V_{DS} (0.2 to 1 V) on I_D-V_{GS} characteristics was studied for S_7 as shown in Fig. 4.13(a). The current level was increased and the Dirac point was shifted rightwards with increase of V_{DS}. The influence of non-linear I_D-V_{DS} of S_7 (Fig. 4.12(e)) is clearly visible on the on/off ratio and g_m as a function of V_{DS} as shown in Fig. 4.13(b) and (c). Though the on/off ratio was increased with V_{DS}, the rate of increment was slow at V_{DS} <0.6 V and fast at V_{DS} >0.6 V. On the other hand, the increment of g_m with V_{DS} was almost saturated at V_{DS} >0.6 V.

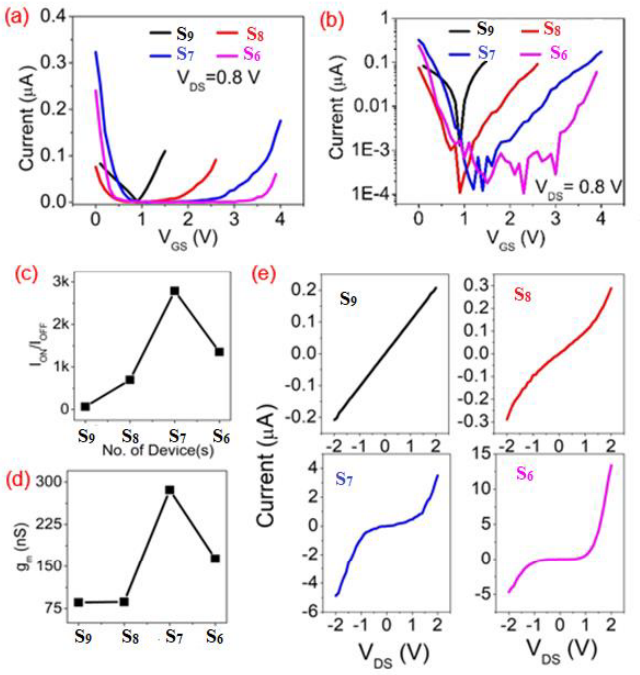

Fig. 4.12. Electrical characteristics of GO-FET (TG0) and three GO/*p*-TiO_2 hybrid FETs (TG0.5, TG1, and TG5) at room temperature (300 K). Drain current as a function of V_{GS} (at V_{DS}=0.8 V) in (a) linear and (b) log scale. (c) On/off ratio (I_{ON}/I_{OFF}) and (d) Transconductance (g_m) for four FETs. (e) Drain current as a function of V_{DS} at normally 'on' condition i.e. V_{GS}=0 V.

The electrical characteristics shown in Fig. 4.12 confirmed the overall performance improvement of GO/*p*-TiO_2 hybrid-FET after incorporation of a certain amount of *p*-TiO_2 nanoparticles in the channel region. The extraordinary enhancement of the on/off ratio in S_7 was the cause of multiple effects i.e. (i) increment of on current at zero gate voltage due to the hole transfer in GO layer from *p*-TiO_2 nanoparticles and (ii) decrease of off current due to increment of barrier potential in GO/*p*-TiO_2/GO junction. The schematic of *p*-TiO_2 nanoparticle decorated GO channel FET is shown in Fig. 4.10(a) where *p*-TiO_2 NPs were placed on both the sides of GO flakes (Fig. 4.14(a)) as observed in the FESEM image in Fig. 4.7. Fig. 4.14(b) and (c) show the hole transfer direction between *p*-TiO_2 and GO layer which has been further authenticated by using an energy band diagram in Fig. 4.14 (d).

Fig. 4.14(d) represents a schematic energy band (EB) diagram of *p*-type GO and *p*-type anatase TiO_2, indicating the interfacial charge transfer possibility among them. EB diagrams was drawn by considering the work function of GO as $q\varphi_g > 4.6\ eV$ [58],[75],[76] and anatase *p*-TiO_2 as $q\varphi_T > 6.95\ eV$ ($q\chi_T + \frac{1}{2} qE_{gT}$) [59],[77]. Energy band gap, calculated from UV Vis spectra was

used to draw the EB diagram in Fig. 4(d). As, $q\varphi_T \gg q\varphi_g$, the electron must flow from GO to p-TiO_2, accumulating the holes in GO at $V_{GS} = 0$ (Fig. 4.14(d)).

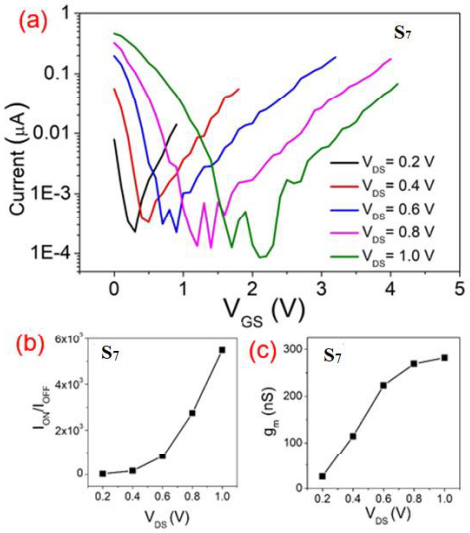

Fig.4.13. (a) I_D-V_{GS} characteristics of S_7 for variable V_{DS} (0.2 to 1 V). (b) On/off ratio ($\frac{I_{ON}}{I_{OFF}}$) and (c) transconductance (g_m) of S_7 as a function of V_{DS}.

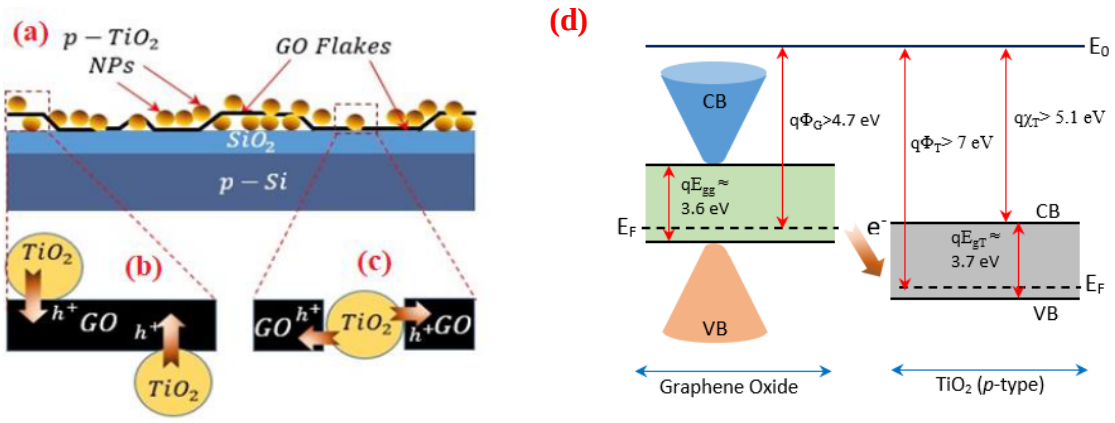

Fig.4.14. (a) A possible side view of the channel region where p-TiO_2 nanoparticles were decorated to both the bottom and top side of GO flakes, as evidenced from the FESEM images. An extended view of (b) GO/p-TiO_2 junctions and (c) GO/p-TiO_2/GO junction showing the hole transfer direction in-between GO and p-TiO_2. (d) Energy band diagram of GO and p-TiO_2 indicating the follow of electron based on the work functions.

Fig. 4.14(a) depicts two possible junctions in the hybrid channel i.e. (i) discrete GO/p-TiO_2 junctions (Fig. 4.14(b)) responsible for the increase of hole concentration in GO layer that increases the on-current at $V_{GS} = 0$ but not playing a significant role in carrier transport at higher V_{GS}between source and drain and (ii) GO/p-TiO_2/GO junctions (Fig. 4.14(c)) which is

playing a significant role in current transport at higher V_{GS} and most importantly restrict the flow of current (off-current) near the Direct point voltage.

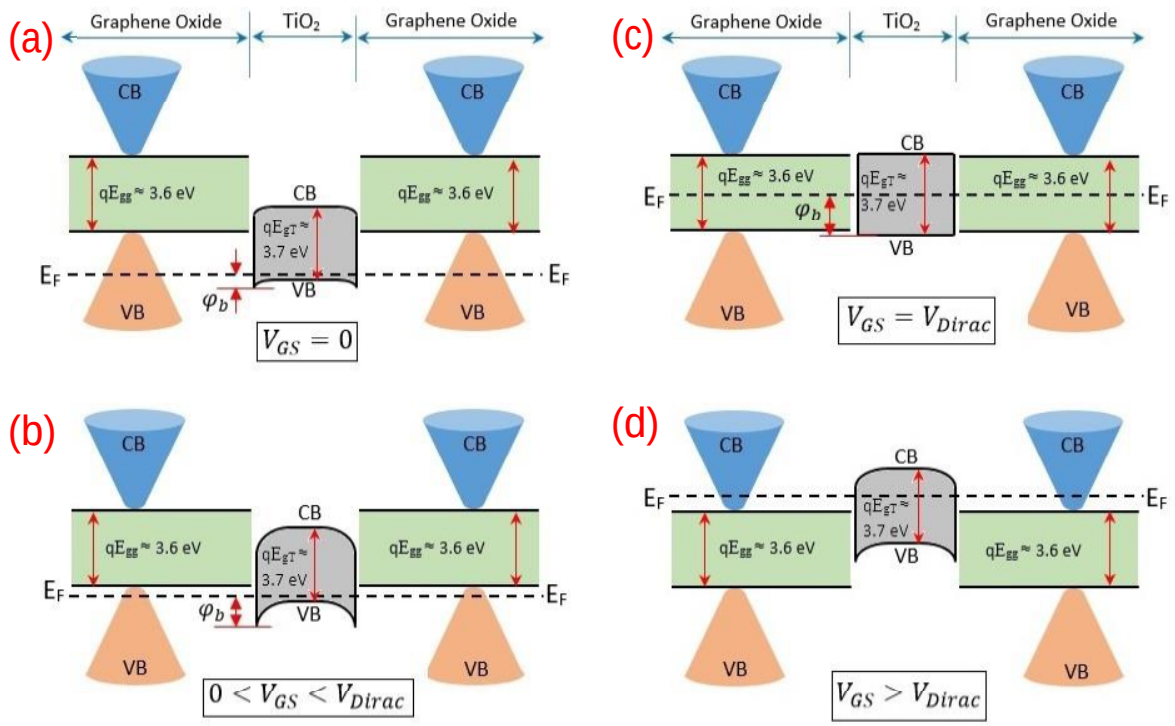

Fig.4.15. A qualitative energy band diagram of GO/*p*-TiO_2/GO junction in equilibrium ($V_{DS} = 0$) for different gate to source voltage (a) V_{GS}=0, (b) $0 < V_{GS} < V_{Dirac}$, (c) $V_{GS} = V_{Dirac}$, (d) $V_{GS} > V_{Dirac}$

Fig. 4.15 exhibits the energy band diagram of GO/*p*-TiO_2/GO junction at different conditions of gate voltage. As the carrier density of *p*-TiO_2 NPs is quite high (in the order of 8×10^{18} cm^{-3} [78]) compared to the GO layer, the shifting of fermi level is more pronounced in GO as shown in Fig. 4.15 (a). Whereas, the band bending in *p*-TiO_2 is negligible indicating a small barrier height (φ_b) at $V_{GS} = 0$. Due to the enhanced hole concentrations in GO and low barrier height in *p*-TiO_2, the amplitude of the on-current at $V_{GS} = 0$ is quite high in the hybrid channel as compared to the pure GO as evident from the $I_D - V_{GS}$characteristics in Fig. 4.12(b). At $0 < V_{GS} < V_{Dirac}$, electrons are injected in GO layer due to the positive field effect and transferred to the *p*-TiO_2 nanoparticles. Electronic exchange is quite easy in-between GO and TiO_2 due to the formation of Ti-O-C linkage as discussed in XPS results in Fig.4.9. As a results, effective hole concentration in GO layer is decreased (fermi level is shifted upward) and the barrier height is increased in *p*-TiO_2 nanoparticles (Fig. 4.15 (b)). With increase of gate voltage further (in positive direction), the drain current is decreased rapidly due these dual effects. At Dirac point ($V_{GS} = V_{Dirac}$), fermi level is aligned exactly at the middle of the GO and *p*- TiO_2 energy

gap as shown in Fig. 4.15 (c). Not only the GO, *p*-TiO_2 also reached at the lowest doping level and restrict the flow of drain current. Also, the barrier height at $V_{GS} = V_{Dirac}$ is maximum in TiO_2 ($\approx \frac{E_{gT}}{2}$=1.85 eV). The off-current in the hybrid channel is now quite low as compared to the pure GO channel due to this high barrier height in TiO_2/GO junction. Beyond the Dirac point i.e. $V_{GS} > V_{Dirac}$, owing to the high field injection of electron, GO as well as TiO_2 NPs behaves like *n*-type semiconductors and the TiO_2/GO behaves like an Ohmic junction (Fig. 4.15 (d)). Drain current increases almost linearly with further increase of V_{GS} in positive direction. So, the above mechanism envisages the effective increment of on-current (at $V_{GS} = 0$) and decrement of off-current (at $V_{GS} = V_{Dirac}$) in case of *p*-TiO_2/GO hybrid-channel FET as compared to the pure GO field effect transistors exhibiting on/off ratio more than 10^3 in order.

For long channel FET, using the drift-diffusion model, mobility can be estimated by Eq.4.6 [79],[80].

$$\mu = \frac{g_m L}{W C_G V_{DS}} \tag{4.6}$$

Using Eq. (2), hole mobility of pure GO-FET (S_7) was calculated as 2.8 cm^2/V-s considering $\frac{L}{W} \approx 1, C_G = 3.835 \times 10^{-8}\, F/cm^2 and\, V_{DS} = 0.8\, V$ where $g_m = 86\, nS$ was taken from Fig. 4.12(d). The mobility of S_7 was also calculated as 9.32 cm^2/V-s considering $g_m = 286\, nS$ (Fig. 4.12(d)). So, the mobility of GO channel was increased almost three times after formation of GO/*p*-TiO_2 hybrid.

4.3.5 VOC sensing

VOC detection at V_{GS} = 0

All the sensors were tested at zero gate voltage (i.e. $V_{GS} = 0\, V$) first that was equivalent to a planer structure of the devices. Among all the nine sensors, S_6 was considered for the selectivity study due to its high bandgap (3.72 eV) and promising morphology where *p*-TiO_2 NPs were decorated with uniform separation on the GO surface (Fig. 4.7 and 4.8). Different groups of VOCs like alcohol (ethanol, methanol and 2 propanol), aldehyde (formaldehyde), ketone (acetone) and aromatic hydrocarbon (xylene) in its 100 ppm concentration were tested by S_6 at 100°C. The transient response in Fig. 4.16(a) and the bar plot in Fig. 4.16(b) envisages the highest response (~30%) of the S_6 towards 100 ppm of ethanol. S_6 also showed an acceptable response towards the other five VOCs. Due to the ethanol selective behaviour of *p*-TiO_2/GO

nanocomposites, the rest of the sensor study was performed by considering ethanol as the target VOC.

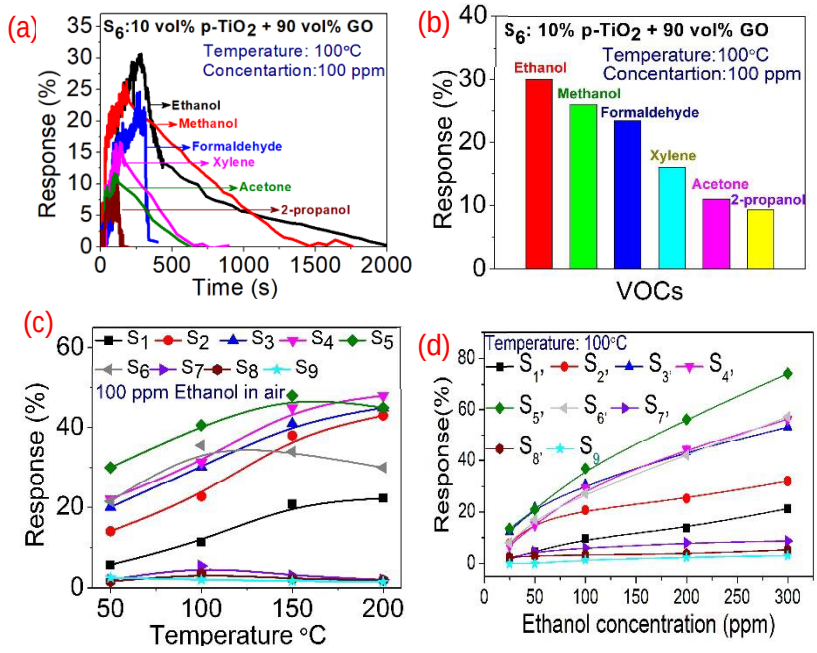

Fig. 4.16. Response characteristics of S_1 to S_9 in two terminal form where V_{DS} = 0.5 V and V_{GS}=0 V were used. (a) S_6 was considered for the selection of VOC mostly sensitive among different group of VOCs. (b) Response magnitude was calculated from part (a) where S_6 exhibited ethanol selective response. (c) Effect of variable operating temperature (50°C to 200°C) on S_1-S_9 in the exposure of 100 ppm of ethanol. (d) Effect of variable concentration of ethanol (25 ppm to 300 ppm) on S_1-S_9 operated at 100°C.

Sensors (S_1-S_9) were tested under the temperature range of 50°C to 200°C in the exposure of 100 ppm ethanol as shown in Fig. 4.16(c). Response of TiO_2 dominated samples (S_1-S_5) was increased linearly from 50°C to 150°C and saturated above 150°C. On the other hand, GO dominated samples (S_6-S_9) showed peak response at 100°C. However, 100°C was considered as the optimized operating temperature to give more emphasis to the GO dominated sensors to study the field effect on VOC sensing. At 100°C, response was increased from S_1 to S_5 and then decreased gradually from S_6 to S_9 (Fig. 4.16(c)). Among all the nine sensors, S_5 exhibited highest response (~40% at 100°C in 100 ppm ethanol) at $V_{GS} = 0\,V$. Response of all the sensors were increased monotonically with increase of ethanol concentration from 25 ppm to 300 ppm as shown in Fig. 4.16(d).

The transient response of all the sensors (S_1 to S_9) within the ethanol concentration range of 25 ppm to 300 ppm were tested at 100°C and represented in Fig. 4.17. Current was decreased in the exposure of reducing vapor ethanol for all the sensors confirming the hole majority in S_1 to S_9. Pure TiO_2 NPs (S_1) in current study exhibited *p*-type conductivity due to the availability of

excess oxygen that declined the oxygen vacancy (V_O) significantly. Therefore, the number of holes contributed by the titanium vacancy (V_{Ti}) became greater than the number of electrons donated by the V_O and the current conduction was started through hole in the TiO_2 NPs [26],[73].

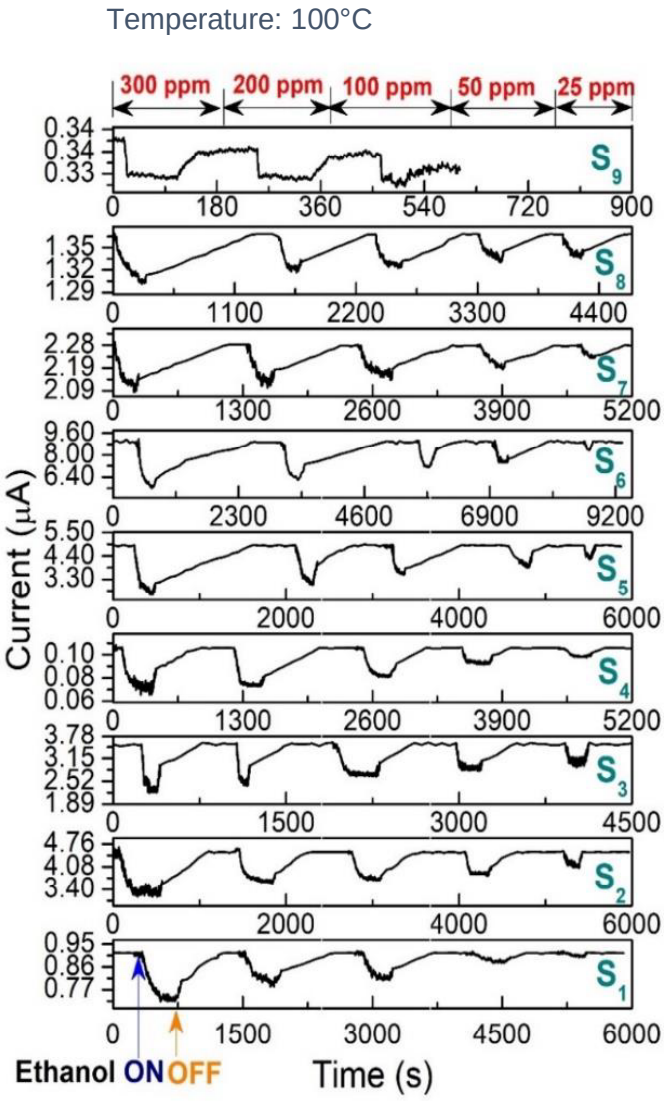

Fig. 4.17. Transient response of S_1-S_9 sensors within the ethanol concentration range of 25 to 300 ppm at 100°C where $V_{DS} = 0.5\,V\ and\ V_{GS} = 0$.

On the other hand, surface adsorption of oxygen species reduces the effective electron concentration in GO (S_9) that is responsible for the *p*-type conductivity in GO [75],[81].

In reducing ambient, electrons are donated to the surface of *p*-TiO_2 NPs (S_1) or GO (S_9), fraction of holes are recombined and current level is decreased as shown in transient behaviour in Fig. 4.17. However, the composites of *p*-TiO_2 NPs and *p*-GO of any ratio (S_2-S_8) showed *p*-type conductivity confirmed from the transient behaviour in Fig. 4.17 where the current was

decreased in the exposure of reducing vapor ethanol. When S_1-S_8 sensors showed response under dynamic range of 25 to 300 ppm, pure GO sensor (S_9) was unable to show response below 100 ppm. All the sensors exhibited a stable baseline with a repeatable sensing behaviour (Fig. 4.17).

VOC detection under positive gate bias ($V_{GS} > 0$)

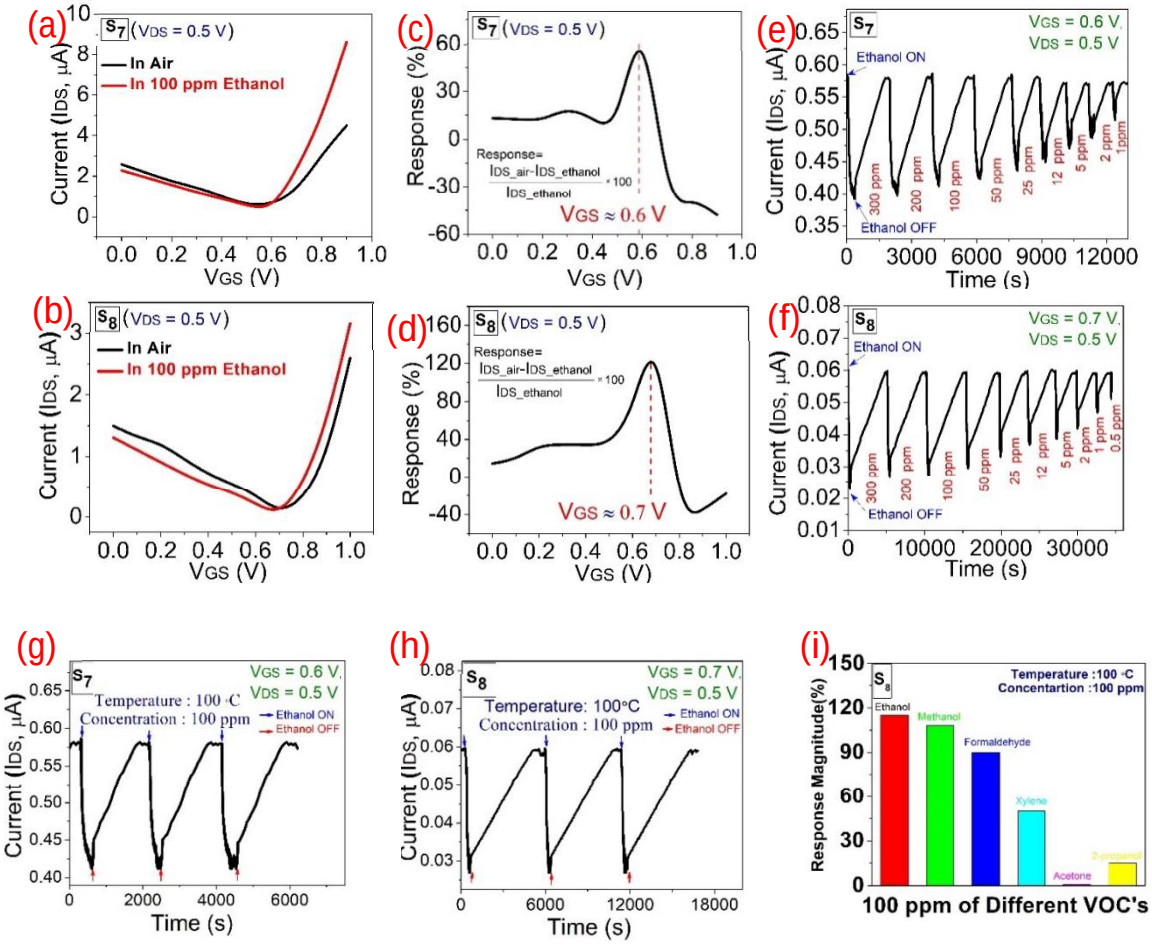

Fig. 4.18. I_{DS}- V_{GS} Characteristics in air and 100 ppm ethanol at 100°C for (a) S_7 and (b) S_8. Response calculated from I_{DS}-V_{GS} characteristics by using the expression $\left[\frac{(I_{DS\_air}-I_{DS\_ethanol})}{I_{DS\_ethanol}}\right] \times 100$ for (c) S_7 and (d) S_8. Amplified transient response of (e) S_7 with $V_{GS} = 0.6\,V$ and (f) S_8 with $V_{GS} = 0.7\,V$. Repeated cycles for 100 ppm of ethanol at 100 °C (g) S_7 with $V_{GS} = 0.6\,V$ and (h) S_8 with $V_{GS} = 0.7\,V$. (i) S_8 sensor representing the selective nature towards ethanol in comparison to other VOCs at $V_{GS} = 0.7\,V$.

As described in section 3.3.4 (Electrical characterization), the field effect was studied for all the FET sensors (S_1 to S_9) where only GO dominated samples (S_4 to S_9) exhibited ambipolar behaviour in the transfer characteristics (I_{DS}- V_{GS}) for various V_{DS} (0.2 to 1 V) as shown in Fig. 4.11.Though the S_7, S_8 and S_9, all the three FETs exhibited strong control of the gate voltage over the current in the channel, only S_7 and S_8 were considered for field assisted VOC sensing

because of following reasons; (i) very poor response (~1.52%) in S_9 and no response was observed below 100 ppm ethanol and (ii) S_7 and S_8 showed small but finite response throughout the ethanol concentration range of 25 ppm to 300 ppm as shown in Fig. 4.17.

I_{DS}- V_{GS} characteristics were measured for S_7 and S_8 in two different ambient i.e. air and 100 ppm ethanol at $V_{DS} = 0.5\,V$ at 100°C and represented in Fig. 4.18(a) and 4.18(b) respectively. Corresponding response magnitude was calculated for variable V_{GS} for S_7 and S_8 and plotted in Fig. 4.18(c) and 4.18(d) respectively. A response peak with ~50% magnitude was observed at $V_{GS} = 0.6\,V$ for S_7 and a response peak with ~120% magnitude was observed at $V_{GS} = 0.7\,V$ for S_8. So, the study confirms that the response magnitude is amplified at particular gate voltage. Now, the transient response was measured for S_7 and S_8 applying $V_{GS} = 0.6\,V$ and $0.7\,V$ respectively while $V_{DS} = 0.5\,V$ was common for both the samples. Amplified transient behavior of S_7 (Fig. 4.18(e)) showed 41% response in the 100 ppm ethanol and the sensor was able to detect minimum 1 ppm of ethanol at 100°C. 115% amplified response was recoded for S_8 (Fig. 4.18(f)) in 100 ppm ethanol and the sensor was successful to detect minimum 500 ppb of ethanol at 100°C.

Sensors showed a stable nature at higher gate to source voltage (or optimized V_{GS}). The repeatable nature of S_7 and S_8 is represented in Fig. 4.18(g) and (h), respectively. Three continuous cycles were taken in exposure to 100 ppm of ethanol for S_7 and S_8 $V_{GS} = 0.6\,V$ and $0.7\,V$ respectively.

S_8 sensor was exposed to 100 ppm of different volatile organic compounds vapours like ethanol, methanol, formaldehyde, acetone and 2-propanol to observe the selective behaviour of FET device at optimized V_{GS} i.e. 0.7 V. The response magnitude towards almost every VOC was enhanced due to the sensitivity amplification. However, no significant increment in the response magnitude was observed in case of acetone. S_8 sensor was still selective towards the ethanol under positive gate bias i.e. V_{GS}=0.7 V (Fig. 4.18(i)).

The amplified response for S_7 and S_8 at higher V_{GS} as compared to the response at $V_{GS} = 0$ is represented in Fig. 4.19(a) and 4.19(b) respectively. A significant increment in the response magnitude was observed at higher V_{GS} as compared to the $V_{GS} = 0$ for both the sensors. Therefore, sensors were capable to detect ethanol of lower concentration at the appropriate gate voltage. ~7 and ~34 time increment in the response magnitude at $V_{GS} = 0.6\,V$ and $0.7\,V$ were recorded for S_7 and S_8 at 100 ppm ethanol respectively (Fig. 4.19(a) and (b)).

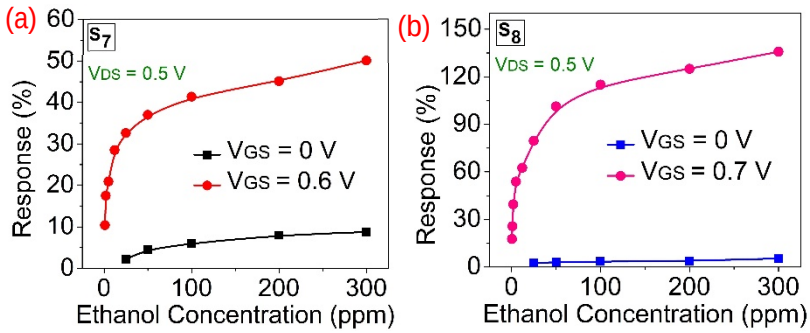

Fig.4.19. Comparative response magnitude between two terminal ($V_{GS} = 0\ V$) and three terminal FET ($V_{GS} > 0\ V$) as a function of ethanol concentration for (g) S_7 and (h) S_8.

4.3.6 Sensing mechanism

In the *p*-TiO_2/GO hybrid channel, two possible junctions were formed i.e. (i) intergranular junctions between *p*-TiO_2 nanoparticles and (ii) heterojunctions between *p*-TiO_2 NPs and *p*-GO flakes. The energy band (EB) diagram of both the junctions were drawn by considering work function of GO $q\varphi_{GO} > 4.5\ eV$ [58] and anatase *p*-TiO_2 $q\varphi_{TiO2} > 6.95\ eV$ $(5.1 + 1/2\ E_g\ eV)$ [59]. Energy band gap of 3.6 eV for pure GO (S_9) and 3.7 eV for pure TiO_2 (S_1) were estimated from UV Vis spectra in Fig. 4.8(d).

VOC sensing in TiO_2 nanoparticles dominated samples are principally controlled by the intergranular junctions between *p*-TiO_2 nanoparticles as discussed in section 3.3.3 of chapter 3.

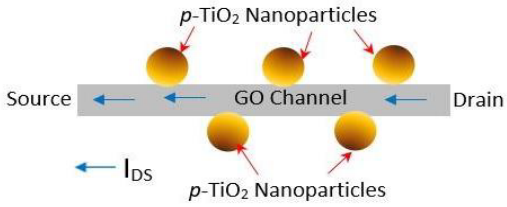

Fig.4.20. Schematic of GO channel decorated with distinct *p*-type TiO_2 NPs indicating the drain current in the channel.

p-TiO₂ /p-GO heterojunctions

A schematic of back gated FET is shown in Fig. 4.10 where the GO channel was implanted with *p*-TiO_2 nanoparticles. Heterojunctions between GO and *p*-TiO_2 NPs is formed transferring the hole from *p*-TiO_2 to *p*-GO ($q\varphi_{GO} < q\varphi_{TiO2}$) that results in a hole accumulation in GO (Fig. 4.21(a)). However, GO layers are 2D in nature with very few in number having very small carrier density. Due to having only surface in GO (no bulk), carrier density of the whole GO layer was assumed to be changed due to formation of heterojunction with *p*-TiO_2.

Owing to the transfer of holes in GO from *p*-TiO_2, Fermi level in GO was shifted downwards in air ambient as shown in Fig. 4.21(a). So, the hole density was increased in GO in air due to (i) adsorption of oxygen species to the GO surface and (ii) the adsorption of oxygen ions to the *p*-TiO_2 NPs surface and further transfer of hole to the GO. As the surface interactions sites are large in number in TiO_2 compared to the GO, heterojunctions can play a significant role in VOC sensing in GO dominated samples. In VOC ambient, holes are extracted directly from GO or through *p*-TiO_2 NPs. So, the hole concentration must be reduced in GO channel shifting the Fermi level upward, lowering the drain current (I_{DS}) in the exposure of VOC as shown in Fig. 4.21(a). High-density conductivity $\sigma(p_{air})$ in GO is considered as proportional to the effective carrier density (holes) p_{air} assuming a constant mobility μ [82],[83]. Considering, $I_{DS\_air} \propto \sigma(p_{air})$ at constant V_{DS} , sensitivity (S_G) of the GO channel at V_{GS} =0 is represented as in Eq.4.7 where p_{air} and p_{VOC} are the hole concentration in the GO channel in air and VOC ambient respectively.

$$S_G(V_{GS}=0) = \left[\frac{I_{DS\_air}(V_{GS}=0) - I_{DS\_VOC}(V_{GS}=0)}{I_{DS\_VOC}(V_{GS}=0)}\right] \times 100 \approx \left[\frac{p_{air}(V_{GS}=0) - p_{VOC}(V_{GS}=0)}{p_{VOC}(V_{GS}=0)}\right] \times 100 \quad (4.7)$$

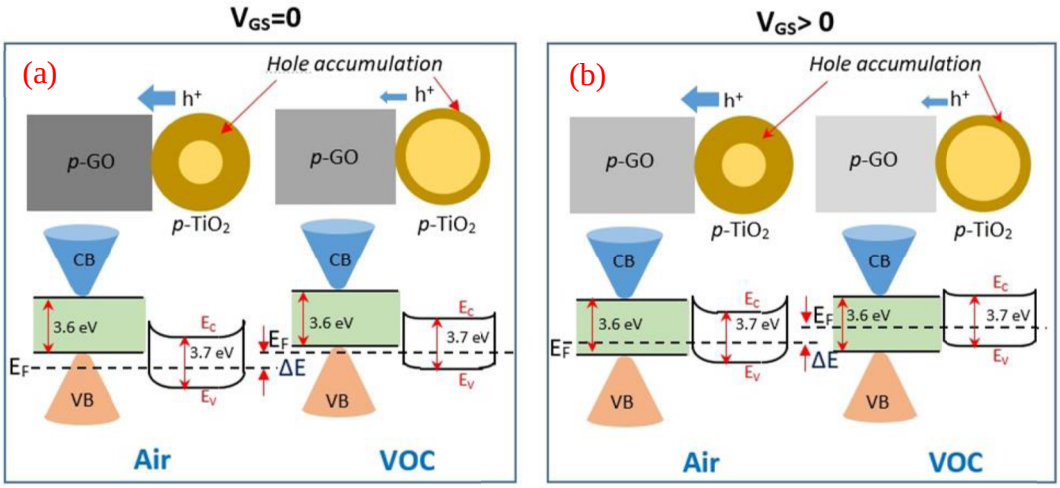

Fig. 4.21. Energy band diagram of GO/*p*-TiO_2 heterojunction at (a) zero gate voltage ($V_{GS}=0$) and (b) positive gate voltage ($V_{GS}>0$) for both the air and VOC ambient.

Now, the VOC sensing behaviour of all the sensors (S_1 to S_9) tested at $V_{GS}=0$ in 100 ppm ethanol at 100°C represented in Fig. 4.16(c) and (d) and Fig. 4.17 can correlate with the formation of these two junctions. ~10% response was recorded for pure *p*-TiO_2 sensor (S_1) which was the only contribution of intergranular junctions between *p*-TiO_2 NPs. Intergranular

junctions in *p*-TiO_2 NPs were dominated in S_1 to S_5 and mostly contributed in VOC sensing**.** The sensor response was increased progressively from S_1 to S_5 due to increase of GO in the sensing layer that eventually increased the additional *p*-TiO_2/GO heterojunctions that contributed in VOC sensing along with the intergranular junctions. S_5 exhibited the highest response of ~40% where both the junctions played a significant role in VOC detection. However, intergranular junctions were not formed in S_6 to S_8 due to large separation between nanoparticles on GO surface (Fig. 4.20). So, the sensor response started to decrease from S_6 to S_9 due to gradual decrease of *p*-TiO_2 ratio as well as the density of *p*-TiO_2/GO heterojunctions in the channel region. The pure GO (S_9) showed lowest response (~1.52%) due to unavailability of any heterojunctions.

Sensitivity amplification by field effect

Response of S_7 and S_8 sensors were further increased by using positive gate voltage ($V_{GS}>0$) as shown in Fig. 4.18 and 4.19. FESEM image in Fig. 4.7 confirmed that the *p*-TiO_2 NPs were very limited in number in S_7 and S_8 and distributed discreetly over the GO channel. So, the drain current was solely flow through the GO channel where discrete heterojunctions of *p*-TiO_2 NPs/GO influenced the gas/VOC interaction to the surface for these S_7 and S_8 samples (Fig. 4.20). At $V_{GS}=0$, Fermi level shifting in GO channel was estimated as ΔE due to the change of ambient from air to VOC and represented in Fig. 4.21(a). At $V_{GS}>0$, additional electrons $[n(V_{GS})]$ were injected to the channel through field effect and the Fermi level in GO was shifted upward lowering the effective hole concentration as well as drain current (I_{DS_air}) in air ambient as shown in the EB diagram in Fig. 4.21(b). Due to the change of ambient from air to VOC, a fraction of holes were extracted further through *p*-TiO_2 NPs/GO heterojunctions and the Fermi level was shifted upward of ΔE amount. So, the effective hole concentration in GO was decreased further in VOC ambient lowering the drain current (I_{DS_VOC}). So, the effective hole concentration in GO channel in four different conditions can be written as $p_{air}(V_{GS}=0) > p_{VOC}(V_{GS}=0) > p_{air}(V_{GS}>0) > p_{VOC}(V_{GS}>0)$ and $I_{DS\_air}(V_{GS}=0) > I_{DS\_VOC}(V_{GS}=0) > I_{DS\_air}(V_{GS}>0) > I_{DS\_VOC}(V_{GS}>0)$. Now, the similar expression of sensitivity like Eq.4.7 can be written in Eq.4.8 considering $V_{GS}>0$.

$$S_G(V_{GS}>0) = \left[\frac{I_{DS\_air}(V_{GS}>0)-I_{DS\_VOC}(V_{GS}>0)}{I_{DS\_VOC}(V_{GS}>0)}\right]\times 100 \approx \left[\frac{p_{air}(V_{GS}>0)-p_{VOC}(V_{GS}>0)}{p_{VOC}(V_{GS}>0)}\right]\times 100 \quad (4.8)$$

However, surface interactions of gas/VOCs are not influenced by the gate voltage directly. So, it can be assumed $\left[I_{DS\_air}(V_{GS}=0) - I_{DS_{VOC}}(V_{GS}=0)\right] \approx \left[I_{DS\_air}(V_{GS}>0) - I_{DS\_VOC}(V_{GS}>\right.$

$0)]$. But, the drain current in VOC ambient is much smaller at $V_{GS}>0$ compared to the $V_{GS}=0$ i.e. $I_{DS\_VOC}(V_{GS} > 0) < I_{DS\_VOC}(V_{GS} = 0)$. So, the response magnitude must be amplified at a certain positive gate voltage ($V_{GS}>0$). Based on the above mechanism, ethanol sensitivity in S_8 was amplified ~34 times at $V_{GS}=0.7\ V$ compared to the $V_{GS}=0$.

4.4 Conclusions

Electrochemical anodization technique was applied to develop pure TiO_2 nanotube array and graphene oxide loaded TiO_2 nanotube array. Uniform graphene doping inside the TiO_2 nanotubes was obtained without hampering the original morphology of the nanotubes. Pure and graphene oxide loaded TiO_2 nanotube array sensor was fabricated in MIM structure where Au is considered as the top electrode and Ti is considered as the bottom electrode. Pure TiO_2 nanotube array depicted a response magnitude of 20% with slow response time (116 s) and recovery time (576 s) to 100 ppm methanol at room temperature. Graphene oxide loaded TiO_2 nanotube array depicted a better response magnitude of 28 % with quick response time (34 s) and recovery time (40 s) to 100 ppm of methanol at room temperature.

The sol-gel derived *p*-TiO_2 nanoparticles (NPs) implanted few layer graphene oxide (GO) field effect transistors were fabricated. Total nine samples (S_1 to S_9) were synthesized where S_1 and S_9 were pure *p*-TiO_2 NPs and pure GO respectively and *p*-TiO_2 NPs ratio in GO was decreased gradually from S_2 to S_8. All the sensors (S_1 to S_9) were tested at (i) zero gate voltage ($V_{GS} = 0$) and (ii) positive gate voltage ($V_{GS} > 0$). At $V_{GS} = 0$, S_5, having 50 vol% *p*-TiO_2 and 50 vol% GO (0.2 wt%) exhibited best response of ~40% among all the nine samples in 100 ppm ethanol at 100°C. Both intergranular junctions between *p*-TiO_2 NPs and *p*-TiO_2 NPs/GO heterojunctions played significant role to enhance the sensitivity in S_5. Among all the nine sensors, GO dominated samples i.e. S_7, S_8 and S_9 exhibited appropriate ambipolar behaviour in the transfer characteristics ($I_{DS} - V_{GS}$) indicating strong field effect over the channel. As the ethanol sensitivity was too poor in S_9 (pure GO), only S_7 (5 vol% *p*-TiO_2+95 vol% GO) and S_8 (1 vol% *p*-TiO_2+99 vol% GO) were considered for the VOC sensing under field effect (i.e. $V_{GS} > 0$). S_7 and S_8 exhibited 41% and 115% response at V_{GS}=0.6 V and 0.7 V respectively in the exposure of 100 ppm ethanol, at 100°C under application of $V_{DS} = 0.5\,V$. The response magnitude of S_7 and S_8 was amplified almost 7 and 34 times at $V_{GS} = 0.6\,V$ and $0.7\,V$ as compared to the zero gate voltage condition ($V_{GS} = 0$). Due to the amplification of response magnitude at positive gate bias, lower detection limit of S_7 and S_8 were extended up to 1 ppm and 500 ppb respectively. Moreover, S_7 exhibited on/off current ratio of 2.8×10^3 (I_{ON} at V_{GS}=0

V and I_{OFF} at V_{GS}=1.2 V), the acceptable transconductance of 0.286 µS and high transport gap of 54.2 meV at room temperature.

Fullerene, the third allotrope of carbon having a cage like structure exists in different forms like -C_{60}, C_{70}, C_{20}. Multiple properties of fullerene have prompted researchers to explore its properties in different fields but a very few experiments are carried out on fullerene or fullerene-nanocomposite based chemical sensors. Different types C_{60}-TiO_2 nanostructure composites can be synthesized and utilized for VOC sensing.

References

1. A. Fattah, S. Khatami, M. Mayorga, C Carmen, M. S. Mariana, B. P. Luis, A. Merkoçi, Graphene/silicon heterojunction schottky diode for vapors sensing using impedance spectroscopy, Small 10 (2014**)** 4193-4199.
2. A. Ye, W. Fan, Q. Zhang, W. Deng, Y. Wang, CdS–graphene and CdS–CNT nanocomposites as visible-light photocatalysts for hydrogen evolution and organic dye degradation, Catalysis Science and Technology 2 (2012) 969-978.
3. Y. Sang, Z. Zhao, J. Tian, P. Hao, H. Jiang, H. Liu, J. P. Claverie, Enhanced photocatalytic property of reduced graphene oxide/TiO_2 nanobelt surface heterostructures constructed by an in situ photochemical reduction method, Small 10 (2014) 3775-3782.
4. G. Neri, S. G. Leonardi, M. Latino, N. Donato, S. Baek, D. E. Conte, P.A. Russo, N. Pinna, Sensing behavior of SnO_2/reduced graphene oxide nanocomposites toward NO_2, Sensors and Actuators B: Chemical 179 (2013) 61-68.
5. M. K. Alam, M. M. Rahman, M. Abbas, S. R. Torati, A. M. Asiri, D. Kim, C. Kim, Ultra-sensitive 2-nitrophenol detection based on reduced graphene oxide/ZnO nanocomposites, Journal of Electroanalytical Chemistry 788 (2017) 66-73.
6. W. Fan, X. Yu, H. C. Lu, H. Bai, C. Zhang, W. Shi, Fabrication of TiO_2/RGO/Cu_2O heterostructure for photoelectrochemical hydrogen production, Applied Catalysis B: Environmental 181 (2016) 7-15.
7. W. K. Jo, H.J. Kang, Titanium dioxide–graphene oxide composites with different ratios supported by Pyrex tube for photocatalysis of toxic aromatic vapors, Powder technology 250 (2013) 115-121.
8. J. H. Lee, A. Katoch, S. W. Choi, J. H. Kim, H. W. Kim, S.S. Kim, Extraordinary improvement of gas-sensing performances in SnO_2 nanofibers due to creation of local

p–n heterojunctions by loading reduced graphene oxide nanosheets, ACS applied materials and interfaces 7 (2015) 3101-3109.

9. E. Lee, D. Lee, J. Yoon, Y. Yin, Y. N. Lee, S. Uprety, Y. S. Yoon, D. J Kim, Enhanced Gas-Sensing Performance of GO/TiO_2 Composite by Photocatalysis, Sensors 18 (2018) 3334.
10. Y. Fan, K. J. Huang, D. J.; Niu, C. P. Yang, Q. S. Jing, TiO_2-graphene nanocomposite for electrochemical sensing of adenine and guanine, Electrochimica Acta 56 (2011) 4685-4690.
11. X. Li, Y. Zhao, X. Wang, J. Wang, A. M. Gaskov, S. A. Akbar, Reduced graphene oxide (rGO) decorated TiO_2 microspheres for selective room-temperature gas sensors, Sensors and Actuators B: Chemical, 230 (2016) 330-336.
12. D. Dutta, S. K. Hazra, J. Das, C. K. Sarkar, S. Basu, Studies on p-TiO_2/n-graphene heterojunction for hydrogen detection, Sensors and Actuators B: Chemical, 212 (2015) 84-92.
13. A. K. Geim, K. S. Novoselov, The rise of graphene. In Nanoscience and technology: a collection of reviews from nature journals, (2010) 11-19.
14. G. Williams, B. Seger, P. V. Kamat, TiO_2-graphene nanocomposites. UV-assisted photocatalytic reduction of graphene oxide, ACS nano 2 (2008) 1487-1491.
15. H. Xu, Z. Zhang, Z. Wang, S. Wang, X. Liang, L. M. Peng, Quantum capacitance limited vertical scaling of graphene field-effect transistor, Acs Nano 5 (2011) 2340-2347.
16. K. P. Loh, Q. Bao, G. Eda, M. Chhowalla, Graphene oxide as a chemically tuneable platform for optical applications Nature chemistry 2 (2010) 1015.
17. D. S. Sutar, G. Singh, V. D. Botcha, Electronic structure of graphene oxide and reduced graphene oxide monolayers, Applied Physics Letters 101 (2012) 103103.
18. W. Choi, I. Lahiri, R. Seelaboyina, Y. S. Kang, Synthesis of graphene and its applications: a review, Critical Reviews in Solid State and Materials Sciences 35 (2010) 52-71.
19. G. Eda, Y. Y. Lin, C. Mattevi, H. Yamaguchi, H. A. Chen, I. S. Chen, C W. Chen, M. Chhowalla, Blue photoluminescence from chemically derived graphene oxide, Advanced materials 22 (2010) 505-509.
20. Y. Sang, Z. Zhao, J. Tian, P. Hao, H. Jiang, H.; Liu, J. P. Claverie, Enhanced photocatalytic property of reduced graphene oxide/TiO_2 nanobelt surface

heterostructures constructed by an in situ photochemical reduction method, Small 10 (2014) 3775-3782.

21. W. Fan, Q. Lai, Q. Zhang, Y. Wang, Nanocomposites of TiO_2 and reduced graphene oxide as efficient photocatalysts for hydrogen evolution, The Journal of Physical Chemistry C 115, (2011) 10694-10701.
22. L. A. Mashat, K. Shin, K. K. Zadeh, J. D. Plessis, S. H. Han, R. W. Kojima, R. B. Kaner, D. Li, X. Gou, S. J. Ippolito, W. Wlodarski, Graphene/polyaniline nanocomposite for hydrogen sensing, The Journal of Physical Chemistry C, 114, (2010) 16168-16173.
23. X. Sun, Z. Liu, K. Welsher, J. T. Robinson, A. Goodwin, S. Zaric, H. Dai, Nano-graphene oxide for cellular imaging and drug delivery, Nano research 1 (2008) 203-212.
24. M. K. Nazarabad, E. K. Goharshadi, M. Aziznezhad, Solar Mineralization of Hard-Degradable Amphetamine Using TiO_2/RGO Nanocomposite, ChemistrySelect 4, (2019) 14175-14183.
25. Y. Fan, H. T. Lu, J. H. Liu, C. P. Yang, Q. S. Jing, Y.X. Zhang, X. K. Yang, K. J. Huang, Hydrothermal preparation and electrochemical sensing properties of TiO_2–graphene nanocomposite, Colloids and Surfaces B: Biointerfaces 83 (2011) 78-82.
26. A. Hazra, K. Dutta, B. Bhowmik, P. Bhattacharyya, Highly repeatable low-ppm ethanol sensing characteristics of p-TiO_2-based resistive devices, IEEE Sensors Journal 15 (2014) 408-416.
27. V. Galstyan, A. Ponzoni, I. Kholmanov, M. M. Natile, E. Comini, S. Nematov, G. Sberveglieri, Reduced graphene oxide–TiO_2 nanotube composite: Comprehensive study for gas-sensing applications, ACS Applied Nano Materials 1 (2018**)** 7098-7105.
28. Z. Ye, H. Tai, R. Guo, Z. Yuan, C. Liu, Y. Su, Z. Chen, Y. Jiang, Excellent ammonia sensing performance of gas sensor based on graphene/titanium dioxide hybrid with improved morphology, Applied Surface Science 419 (2017) 84-90.
29. Y. He, L. Zhu, Y. Liu, J. N. Ma, D. D Han, H. B. Jiang, B. Han, H. Ding, Y. L. Zhang, Femtosecond Laser Direct Writing of Flexible All-Reduced Graphene Oxide FET, IEEE photonics technology letters 28 18 (2016) 1996-1999.
30. J. N. Ma, Y. He, Y. Liu, D. D. Han, Y. Q. Liu, J. W. Mao, H. B. Jiang, Y. L. Zhang, Facile fabrication of flexible graphene FETs by sunlight reduction of graphene oxide Opt. Letters 42 (2017) 3403-3406.

31. Y.L. Zhang, L. Guo, H. Xia, Q.D. Chen, J. Feng, H.B. Sun, Photoreduction of graphene oxides: Methods, properties and application, Advanced Optical Mater 2 (2014) 10–28.
32. R. You, Y. Q. Liu, Y. L. Hao, D. D. Han, Y. L. Zhang, Z. You, Laser fabrication of graphene-based flexible electronics Advanced Materials 32 (2020)1901981, 2020.
33. G. Eda, A. Nathan, P.Weobkenberg, F. Colleaux, K. Ghaffarzadeh, T.D. Anthopoulos, M. Chhowalla, Graphene oxide gate dielectric for graphene-based monolithic field effect transistors Applied Physics Letters 102 (2013) 133108.
34. B. Standley, A. Mendez, E. Schmidgall, M. Bockrath, Graphene−graphite oxide field-effect transistors Nano Letters 12 (2012) 1165–1169.
35. L. Wang, J. Lian, P. Cui, Y. Xu, S. Seo, J. Lee, Y. Chan, H. Lee, Dual n-type doped reduced graphene oxide field effect transistors controlled by semiconductor nanocrystalsw, Chemical Communications 48 (2012) 4052-4054.
36. J. Sun, T. Iwasaki, M. Muruganathan, H. Mizuta, Lateral plasma etching enhanced on/off ratio in graphene nanoribbon field-effect transistor, Applied Physics Letters 106 (2015) 033509.
37. P. Li, R. Z. Zeng, Y. B. Liao, Q. W. Zhang, J. H. Zhou, A Novel, Graphene metal semi-insulator semiconductor transistor and its new super-low power mechanism, Scientific Reports 9 (2019) 3642.
38. T. Kato, R. Hatakeyama, Site- and alignment-controlled growth of graphene nanoribbons from nickel nanobars, Nature Nanotechnology 7 (2012) 651-656.
39. A. Hazra, S. Basu, Graphene nanoribbon as potential on-chip interconnect material—A review, *C*—Journal of Carbon Research 4 3 (2018) 49.
40. Y. W. Son, M.L. Cohen, S.G. Louie, Energy gaps in graphene nanoribbons, Physical Review Letter 97 (2006) 216803.
41. F. Xia, D. B. Farmer, Y-M. Lin, P. Avouris, Graphene field-effect transistors with high on/off current ratio and large transport band gap at room temperature, Nano Letters 10 (2010) 715–718.
42. W.S. Hwang, K. Tahy, X. Li, H. Xing, A.C. Seabaugh, C.Y. Sung, D. Jena, Transport properties of graphene nanoribbon transistors on chemicalvapor-deposition grown wafer-scale graphene, Applied Physics Letters 100 (2012) 203107.
43. D. Choi, C. Kuru, Y. Kim, G. Kim, T. Kim, R. Chen, S. Jin, Uniformly nanopatterned graphene field-effect transistors with enhanced properties, Nanoscale Research Letters 10 (2015) 289.

44. Y. Lu, B. Goldsmith, D.R. Strachan, J.H. Lim, Z. Luo, A. T. Charlie Johnson, High-on/off-ratio graphene nanoconstriction field-effect transistor, Small 6 (2010) 2748–2754.
45. P. Jangid, D. Pathan, A. Kottantharayil, Graphene nanoribbon transistors with high I_{ON}/I_{OFF} ratio and mobility, Carbon 132 (2018) 65-70.
46. Y. Liu, S. Lin, L. Lin, A versatile gas sensor with selectivity using a single graphene transistor, In 2015 Transducers-2015 18th International Conference on Solid-State Sensors, Actuators and Microsystems (TRANSDUCERS) IEEE (2015) 961-964.
47. A. Inaba, K. Yoo, Y. Takei, K. Matsumoto, I. Shimoyama, Ammonia gas sensing using a graphene field–effect transistor gated by ionic liquid, Sensors and Actuators B: Chemical 195 (2014) 15-21.
48. Y. Ren, C. Zhu, W. Cai, H. Li, H. Ji, I. Kholmanov, Y. Wu, R. D. Piner, R. S. Ruoff, Detection of sulfur dioxide gas with graphene field effect transistor, Applied Physics Letters 100 (2012) 163114.
49. G. Lu, K. Yu, L. E. Ocola, J. Chen, Ultrafast room temperature NH_3 sensing with positively gated reduced graphene oxide field-effect transistors, Chemical Communications 47 (2011) 7761-7763.
50. M. Nakamura, Y. Kanai, Y. Ohno, K. Maehashi, K. Inoue, K. Matsumoto, Graphene-FET-based gas sensor properties depending on substrate surface conditions Japanese Journal of Applied Physics 54 (2015) 06FF11.
51. M. Łuszczek, M.; Turzyński, D. Świsulski, Modelling of Graphene Field-Effect Transistor for electronic sensing applications, Przegląd Elektrotechniczny 91 (2015) 170-172.
52. A. Falak, Y. Tian, L. Yan, X. Zhang, L. Xu, Z. Song, F. Dong, P. Chen, M. Zhao, H. Wang, W. Chu Simultaneous achievement of superior response and full recovery of titanium dioxide/graphene hybrid FET sensors for NH_3 through p-to n-mode switch, Physical Chemistry Chemical Physics 22 29 (2020) 16701-16711.
53. S. Li, Y. Weijie, Y. Li, J. Sun, M. Zhu, Z. Liu, T. Deng, High sensitivity ultraviolet detection based on three-dimensional graphene field effect transistors decorated with TiO_2 NPs, Nanoscale 11 31 (2019) 14912-14920.
54. S. Li, T. Deng, Y. Zhang, Y. Li, Weijie Yin, Q. Chen, Z. Liu, Solar-blind ultraviolet detection based on TiO_2 nanoparticles decorated graphene field-effect transistors, Nanophotonics 8 5 (2019) 899-908.

55. Y. H. Wu, P. Y. Tseng, P. Y. Hsieh, H. T. Chou, N. H. Tai, High mobility of graphene-based flexible transparent field effect transistors doped with TiO_2 and nitrogen-doped TiO_2, ACS applied materials & interfaces 7 18 (2015) 9453-9461.
56. P. H. Ho, Y. C. Yeh, D. Y. Wang, S. S. Li, H. A. Chen, Y. H. Chung, C. C. Lin, W. H. Wang, C. W. Chen, Self-encapsulated doping of n-type graphene transistors with extended air stability, ACS nano 6 7 (2012) 6215-6221.
57. K. Zheng, F. Meng, L. Jiang, Q. Yan, H. H. Hng, X. Chen, Visible Photoresponse of Single-Layer Graphene Decorated with TiO_2 Nanoparticles, Small 9 12 (2013) 2076-2080.
58. A.V. Singhal, H. Charaya, I. Lahiri, Noble metal decorated graphene-based gas sensors and their fabrication: a review, Critical Reviews in Solid State and Materials Sciences 42 (2017) 1-28.
59. D. O. Scanlon, C.W. Dunnill, J. Buckeridge, S. A. Shevlin, A. J. Logsdail, S. M. Woodley, C. R. A. Catlow, M. J. Powell, R. G. Palgrave, I. P. Parkin, G. W. Watson, T. W. Keal, P. Sherwood, A. Walsh, A. A. Sokol Band alignment of rutile and anatase TiO_2, Nature materials 12 (2013) 798.
60. P.P Sahay, R. K. Nath, Al-doped ZnO thin films as methanol sensors, Sensors and Actuators B: Chemical 134 2 (2008) 654-659.
61. P. Wang, J. Wang, X. Wang, H. Yu, J. Yu, M. Lei, Y. Wang, One-step synthesis of easy-recycling TiO_2-rGO nanocomposite photocatalysts with enhanced photocatalytic activity, Applied Catalysis B: Environmental 132 (2013) 452-459.
62. H. Zhang, X. Wang, N. Li, J. Xia, Q. Meng, J. Ding, J. Lu, Synthesis and characterization of TiO_2/graphene oxide nanocomposites for photoreduction of heavy metal ions in reverse osmosis concentrate, RSC advances 8 (2018) 34241-34251.
63. X. Pan, Y. Zhao, S. Wang, Z. Fan, TiO_2/graphene nanocomposite for photocatalytic application, Materials and Processes for Energy: Communicating Current Research and Technological Developments; Méndez-Vilas, A., Ed (2013) 913-920.
64. Y. Ni, W. Wang, W. Huang, C. Lu, Z. Xu, Graphene strongly wrapped TiO_2 for high-reactive photocatalyst: A new sight for significant application of graphene, Journal of colloid and interface science 428 (2014) 162-169.
65. Y. Zhang, C. Pan, TiO_2/graphene composite from thermal reaction of graphene oxide and its photocatalytic activity in visible light, Journal of Materials Science 46 (2011) 2622-2626.

66. A. Hazra, B. Bhowmik, K. Dutta, P. P. Chattopadhyay, P. Bhattacharyya, Stoichiometry, length, and wall thickness optimization of TiO_2 nanotube array for efficient alcohol sensing, ACS applied materials & interfaces 7 (2015) 9336-9348.
67. G. Rajender, J. Kumar, P. K. Giri, Interfacial charge transfer in oxygen deficient TiO_2-graphene quantum dot hybrid and its influence on the enhanced visible light photocatalysis, Applied Catalysis B: Environmental 224 (2018) 960-972.
68. T. Lavanya, K. Satheesh, M. Dutta, N. V. Jaya, N. Fukata, Superior photocatalytic performance of reduced graphene oxide wrapped electrospun anatase mesoporous TiO_2 nanofibers, Journal of alloys and compounds 615 (2014) 643-650.
69. J. Zhang, H. Yang, G. Shen, P. Cheng, J. Zhang, S. Guo, Reduction of graphene oxide via L-ascorbic acid, Chemical Communications 46 (2010) 1112-1114.
70. W. Ren, Z. Ai, F. Jia, L. Zhang, X. Fan, Z. Zou, Low temperature preparation and visible light photocatalytic activity of mesoporous carbon-doped crystalline TiO_2, Applied Catalysis B: Environmental 69 (2007) 138-144.
71. J. Zhang, C. Pan, P. Fang, J. Wei, R. Xiong, Mo^+ C codoped TiO_2 using thermal oxidation for enhancing photocatalytic activity, ACS applied materials & interfaces 2 (2010**)** 1173-1176.
72. P. Bindra, S. Gangopadhyay, A. Hazra, Au/TiO_2 Nanotubes/Ti-based solid-state vapor sensor: Efficient sensing in resistive and capacitive modes, IEEE Transactions on Electron Devices 65 (2018**)** 1918-1924.
73. A. Hazra, S. Das, J. Kanungo, C. K. Sarkar, S. Basu, Studies on a resistive gas sensor based on sol–gel grown nanocrystalline p-TiO_2 thin film for fast hydrogen detection, Sensors and Actuators B: Chemical 183 (2013) 87-95.
74. U. Naknikham, V. Boffa, G. Magnacca, A. Qiao, L. R. Jensen, Y. Yue, Mutual-stabilization in chemically bonded graphene oxide–TiO_2 heterostructures synthesized by a sol–gel approach, RSC advances 7 (2017) 41217-41227.
75. S. Perumbilavil, P. Sankar, T.P. Rose, R. Philip, White light Z-scan measurements of ultrafast optical nonlinearity in reduced graphene oxide nanosheets in the 400–700nm region, Applied Physics Letters 107 (2015) 051104.
76. J. Y. Kim, H. S. Jung, J. H. No, J.-R. Kim, and K. S. Hong, Influenceof anatase-rutile phase transformation on dielectric properties of sol-gel derived TiO_2 thin films, J Electroceram 16 (2003) 447–451.

77. A. Hazra, P.P. Chattopadhyay, P. Bhattacharyya, Hybrid fabrication of highly rectifying-homojunction based on nanostructured TiO_2, IEEE Electron Device Letters 36 (2015) 505-507.
78. A. Hazra, P. Bhattacharyya, Role of junction geometry in determining the rectification performance of nanostructured TiO_2-based p-n junctions, IEEE Transactions on Electron Devices 62 (2015) 1984-1990.
79. H. Xu, Z. Zhang, Z. Wang, S. Wang, X. Liang, L-M. Peng, Quantum capacitance limited vertical scaling of graphene field-effect transistor, ACS Nano 5 3 (2011) 2340–2347.
80. M. Dragoman, A. Dinescu, D. Dragoman, Room temperature nanostructured graphene transistor with high on/off ratio, Nanotechnology 28 (2017) 015201.
81. O. Okobiah, R. F. Reidy, Surface interactions: functionalization of graphene oxide and wetting of graphene oxide and graphene, Current Organic Chemistry 20 **(**2016) 674-681.
82. L. Wang, J. Lian, P. Cui, Y. Xu, S. Seo, J. Lee, Y. Chan, H. Lee, Dual n-type doped reduced graphene oxide field effect transistors controlled by semiconductor nanocrystals, Chemical Communications 48 (2012**)** 4052-4054.
83. S. Adam, E. H. Hwang, V. M. Galitski, S. D. Sarma, A self-consistent theory for graphene transport, Proceedings of the National Academy of Sciences 104 (2007) 18392-18397.